CORE-CROWN QUANTUM-WELL NANOPLATELET FUNCTIONALIZED TiO_2 FOR PHOTOCATALYTIC NO_X ABATEMENT

A THESIS SUBMITTED TO
THE GRADUATE SCHOOL OF ENGINEERING AND SCIENCE
OF BILKENT UNIVERSITY
IN PARTIAL FULFILMENT OF THE REQUIREMENTS
FOR THE DEGREE OF
MASTER OF SCIENCE
IN
CHEMISTRY

BY

Elnaz Ebrahimi

July 2020

CORE-CROWN QUANTUM-WELL NANOPLATELET FUNCTIONALIZED TiO_2 FOR PHOTOCATALYTIC NO_X ABATEMENT

By Elnaz Ebrahimi

July 2020

We certify that we have read this thesis and that in our opinion it is fully adequate, in scope and in quality, as a thesis for the degree of Master of Science.

Assoc. Prof. Emrah Özensoy (Advisor)

Prof. Dr. Şefık Süzer

Asst. Prof. Burak Ülgüt

Asst. Prof. Ferdi Karadaş

Prof. Dr. Deniz Üner

Approved for the Graduate School of Engineering and Science

Ezhan Karaşan

Director of the Graduate School

ABSTRACT

CORE-CROWN QUANTUM-WELL NANOPLATELET FUNCTIONALIZED TiO_2 FOR PHOTOCATALYTIC NO_X ABATEMENT

Elnaz Ebrahimi

M.Sc. in Chemistry

Advisor: Emrah Özensoy

July 2020

Oleic acid capped core/crown CdSe/CdSeTe quantum-well nanoplatelets (NPL) were used in the surface functionalization of TiO_2. Structural characterization of the synthesized photocatalytic architecture was carried out to shed light on its surface chemistry, electronic, and crystallographic structure. NPL/TiO_2 composites were tested in NO photo-oxidation under ultraviolet-A (UVA) and visible (VIS) light, showing a remarkable activity in NO_x abatement and high selectivity for nitrate storage as compared to standard benchmark TiO_2 photocatalyst (*i.e.* P25). Improved photocatalytic behavior can be attributed to the decrease in the bandgap and enhanced photogenerated electron-hole pair separation as a result of the incorporation of CdSe/CdSeTe NPL onto TiO_2. Stability of composites was also investigated in durability tests. Even though some decrease in photocatalytic activity and selectivity of NPL/TiO_2 composites was observed, performance of the NPL/TiO_2 composites was found to be significantly better than pure TiO_2.

Keywords: Photocatalytic NO_x abatement, PHONOS, DeNO_x index, titanium dioxide, CdSe/CdSeTe nanoplatelets, quantum-wells.

ÖZET

FOTOKATALİTİK NO_X ARITIMI İÇİN ÇEKİRDEK-ÇEPER YAPILI KUANTUM-KUYU NANOPLAKALARI İLE ZENGİNLEŞTİRİLMİŞ TiO_2 MALZEMELERİ

Elnaz Ebrahimi

Kimya Yüksek Lisans Tezi

Danışman: Emrah Özensoy

Temmuz 2020

Oleik asit ile kaplanmış CdSe/CdSeTe kuantum kuyu nanoplakaları (KKN), TiO_2 yüzeylerinin zenginleştirilmesinde kullanılmıştır. Sentezlenen malzemelerin yüzey kimyasal, kristalografik ve elektronik yapılarının aydınlatılması için karakterizasyon çalışmaları gerçekleştirilmiştir. KKN/TiO_2 kompozitlerin, mor ötesi-A (UVA) ve görünür (VIS) ışık altında, NO foto-oksidasyon tepkimesinde, yüksek dönüşüm ve nitrat depolama seçiciliği gösterdiği ve referans ticari titanya katalizöründen (yani P25'den) daha başarılı olduğu saptanmıştır. KKN/TiO_2 malzemesinin üstün performansı, küçük elektronik bant aralığı ve uzun ömürlü elektron-boşluk çiftlerinin oluşmasıyla açıklanmıştır. Uzun soluklu dayanım testlerinde, KKN/TiO_2 sistemlerinde kısmi olarak bir performans düşüşü ölçülse de; bu sistemlerin performansı, ticari P25 referans fotokalizörünün her zaman üzerinde kalmayı başarmıştır.

Anahtar Kelimeler: Fotokatalitik NO_x arıtımı, PHONOS, DeNO_x indeks, titanyum dioksit, CdSe/CdSeTe nanoplakaları, kuantum kuyuları.

Acknowledgment

I would like to express my sincere gratitude to my advisor Assoc. Prof. Emrah Özensoy for giving me the opportunity to be a part of his research group and providing valuable guidance throughout this research. His guidance and endless motivation have deeply inspired me.

I would also like to offer my special thanks to our collaborator Prof. Hilmi Volkan Demir and his PhD student Farzan Shabani for providing quantum well nanoplatelets.

I am very thankful to all Chemistry department faculty members for providing friendly environment as well as UNAM research center for offering various sources and equipment which I made use of them to full fill my master research.

I would like to extend my gratitude to all past and present lab mates in Özensoy research group; especially PHONOS group; Sean William McWhorter, Merve Balcı, Gökberk Katırcı and İlker Deveci. My Special thanks goes to Dr. Muhammad Irfan, for enlightening me particularly during the initial stages of my research. He always helped and supported me willingly during my research and never stopped inspiring me to learn more and follow my targets. I wish him to have a continuous success in his objectives and a happy and healthy life with his family. Also, I thank my friends, Sinem Gürbüz and Zeynep Kap for all nice and fun times we have had together during these two years and making the lab a nice place to work.

Last but not the least, I would like to thank my family for their continuous prayers, support, caring and unconditional love. And finally, I would like to express my deepest thank to my husband Sina Sadigh Akbari, for all his understanding and motivation. Without his support I would be lost during the difficult times I was spending away of my parents and country.

List of Figures

List of Tables

1 Introduction

1.1 Air Pollution

Relationship between humans and their environment involves a delicate balance. The population of the world has progressively risen since the modernization and industrial revolution, and with population growth, the ecosystem has been tremendously affected. The air we breathe is one of the most precious resources. However, it is contaminated with natural sources (*e.g.* volcanic eruptions, soil erosion and forest fires) as well as anthropogenic emissions (agricultural activities, combustion of fossil fuels and industrial exhaust) which are endangering human health, animal life and the environment [1]. Many regulations and studies are taken into consideration by environmental agencies to control and reduce the harmful pollutants in the atmosphere. United States Environmental Protection Agency (EPA) has set ambient air quality standards for six common air pollutants including sulfur dioxide, carbon monoxide, lead, ground level ozone, particulate matter and nitrogen dioxide [2].

Atmospheric pollutants can be classified into two categories. Pollutants such as carbon monoxide (CO), sulfur dioxide (SO_2), volatile organic compounds (VOC) and nitrogen oxides (NO_x) that are released directly from the source into the atmosphere are known as the primary pollutants. The other category involves pollutants generated by subsequent chemical reactions in the atmosphere and these pollutants are called secondary pollutants (*e.g.* tropospheric ozone (O_3), acid rain containing HNO_3, and H_2SO_4) [3].

1.1.1 NO_x Emission

Of all gas contaminants, nitrogen oxides (NO_x), are among the most harmful atmospheric pollutant gases. Although environmental protection agencies set a value of ≤ 0.2 ppm for NO_x emissions, it is often exceeded in urban settings [4]. Different types of nitrogen oxides such as N_2O, NO, NO_2, N_2O_3, N_2O_4, and N_2O_5 can exist in the atmosphere. Various properties of nitrogen oxide compounds are listed in Table 1.1.

Table 1.1: Nitrogen oxide and their properties. Adapted from Ref [5].

Formula	Name	Nitrogen Valence	Properties
N_2O	nitrous oxide	1	colorless gas water soluble
NO N_2O_2	nitric oxide dinitrogen dioxide	2	colorless gas slightly water soluble
N_2O_3	dinitrogen trioxide	3	black solid water soluble, decomposes in water
NO_2 N_2O_4	nitrogen dioxide dinitrogen tetroxide	4	red-brown gas very water soluble, decomposes in water
N_2O_5	dinitrogen pentoxide	5	white solid very water soluble, decomposes in water

The term NO_x usually refers to nitrogen monoxide (NO) and nitrogen dioxide (NO_2). NO_x species are poisonous and are also highly reactive. Therefore, they can contribute to the formation of secondary air pollutants via numerous reactions in air. Furthermore, human respiratory and immune systems are severely affected by NO and NO_2 [6].

1.1.2 Formation of Secondary Air Pollutants due to NO_x Compounds

- **Ground Level Ozone:** The ozone layer is a part of the atmosphere, containing relatively high concentration of O_3. It is mainly found in the lower part of the stratosphere and plays a crucial role as a natural UV irradiation shield for earth [7], [8]. However, accumulation of ozone close to the sea level, which is called the "ground level ozone" is undesirable which can lead to detrimental effects on lung tissue and loss of respiratory function, especially in vulnerable populations (children, elderly people, asthmatics). Ground level ozone formation occurs by the chemical reaction of NO_x, VOCs and CO generated by man-made sources in the presence of sunlight. Rate of ground level ozone formation is also influenced by the rate of the initial reaction between VOCs or CO with hydroxyl radicals ($^{\bullet}OH$). Reactions (1-6) summarize the simplified chemical pathways of ground level ozone formation [9]–[11].

$$VOC + {}^{\bullet}OH \longrightarrow RO_2^{\bullet} + H_2 \quad (1)$$

$$CO + {}^{\bullet}OH\ (+ O_2) \longrightarrow HO_2^{\bullet} + CO_2 \quad (2)$$

$$RO_2^{\bullet} + NO \longrightarrow VOC + H_2O + NO_2 \quad (3)$$

$$HO_2^{\bullet} + NO \longrightarrow OH + NO_2 \quad (4)$$

$$NO_2 + hv \longrightarrow NO + O^{\bullet} \quad (5)$$

$$O + O_2 + M \longrightarrow O_3 + M \quad (6)$$

- **Acid Rain:** While rain may help to eliminate air contaminants from the atmosphere, NO_2 may also be dissolved in rain to produce highly corrosive nitrous acid (HNO_2) and nitric acid (HNO_3). The reactions during the formation of acid rain are given below [12].

$$VOC + {}^{\bullet}OH \longrightarrow RO_2^{\bullet} + H_2 \quad (7)$$

$$4NO + 3O_2 + 2H_2O \rightarrow 4HNO_3 \quad (8)$$

$$4NO_2 + 2H_2O + O_2 \rightarrow 4HNO_3 \quad (9)$$

$$3NO_2 + H_2O \rightarrow 2HNO_3 + NO \quad (10)$$

- **Smog:** Interest in the control of NO_x emissions has continuously grown since 1952, *i.e.* after the role of atmospheric NO_x species in the development of photochemical smog was proposed by Haagen-Smit in Los Angeles, USA [13]. Smog is a combination of smoke (*i.e.* aerial CO, particulate matter and VOCs) and fog (*i.e.* a visible aerosol containing aerial microscopic water droplets or ice) that is generated when high levels of emissions are combined with fog. As sunlight meets a mixture of NO_2 and unburned hydrocarbons in the atmosphere, photochemical smog is formed.

1.1.3 NO_x Sources

NO_x can be emitted to the atmosphere from mobile sources (*e.g.* vehicles, engines, marine vessels, *etc.*) or stationary sources (*e.g.* power plants, chemical plants, refineries, cement plants, foundries, manufacturing plants, *etc.*) Figure 1.1 shows distribution of NO_x emissions among various sectors in Europe (2011) [14].

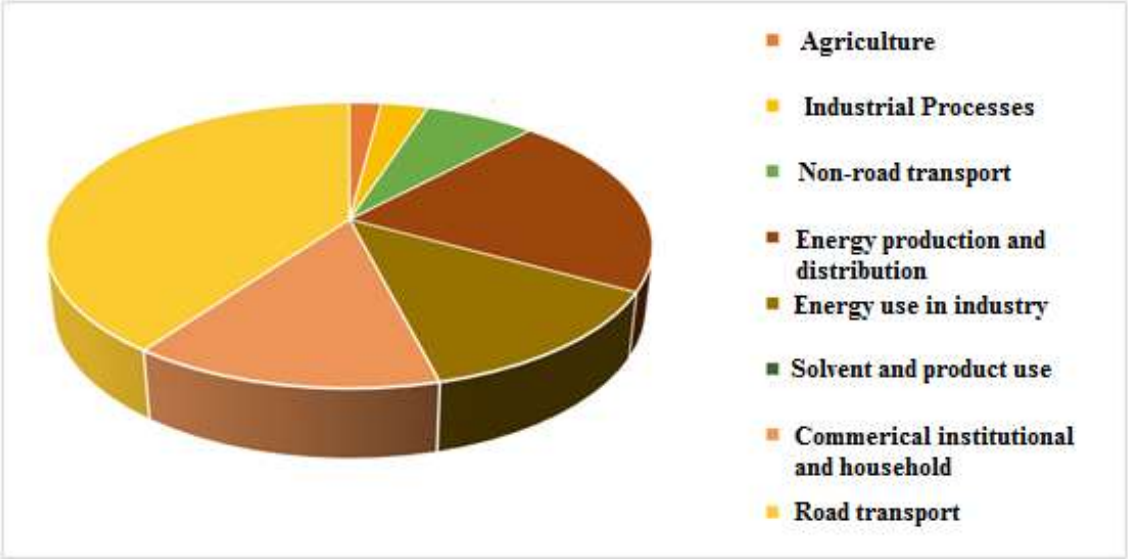

Figure 1.1: Distribution of NO_x emissions among different sectors in EU (2011). Adapted from Ref [14].

Primary mechanisms of NO_x formation can be categorized in three groups:

1.1.3.1 Thermal NO_x

Thermal NO_x is formed by the reaction of atmospheric oxygen, nitrogen, and also hydroxyl radicals (which are abundant in a flame) at elevated temperatures through a pathway first suggested by Zeldovich in 1947 [15][16]. The reactions are extremely temperature reliant, therefore higher the combustion temperature, the more NO_x is formed.

$$N_2 + O \longrightarrow NO + N \quad (11)$$

$$N + O_2 \longrightarrow NO + O \quad (12)$$

$$N + OH \longrightarrow NO + H \quad (13)$$

1.1.3.2 Fuel NO_x

This form of NO_x forms by the oxidation of nitrogen containing organic compound in fuels through the reaction 14 [8].

$$R_xN_y + O_2 \longrightarrow NO, NO_2, CO_2, H_2O \qquad (14)$$

For high- quality gaseous fuels which are free of nitrogen containing compounds, the fuel NO_x is not a concern. However, in the case of liquid and solid fuels containing large amounts nitrogen enormous amounts of NO_x can be formed via reaction (14) [8].

1.1.3.3 Prompt NO_x

Prompt NO_x is the product of the fast reaction between atmospheric nitrogen and hydrocarbon radicals in the earliest stages of combustion at lower temperatures. This kind of NO_x is less of importance compared to others and it becomes predominant under fuel-rich conditions [8].

1.1.4 Approaches for NO_x Removal

NO_x control techniques can be divided into primary and secondary procedures shown in Figure 1.2. Primary methods of NO_x removal also known as pre-combustion methods, are mostly applied in the combustion zone by adjusting the combustion parameters to reduce NO_x formation without the need for another reactor. Whereas the secondary methods (*i.e.* post-combustion processes) are based on chemical reactions in order to decrease NO_x species that are already formed [17].

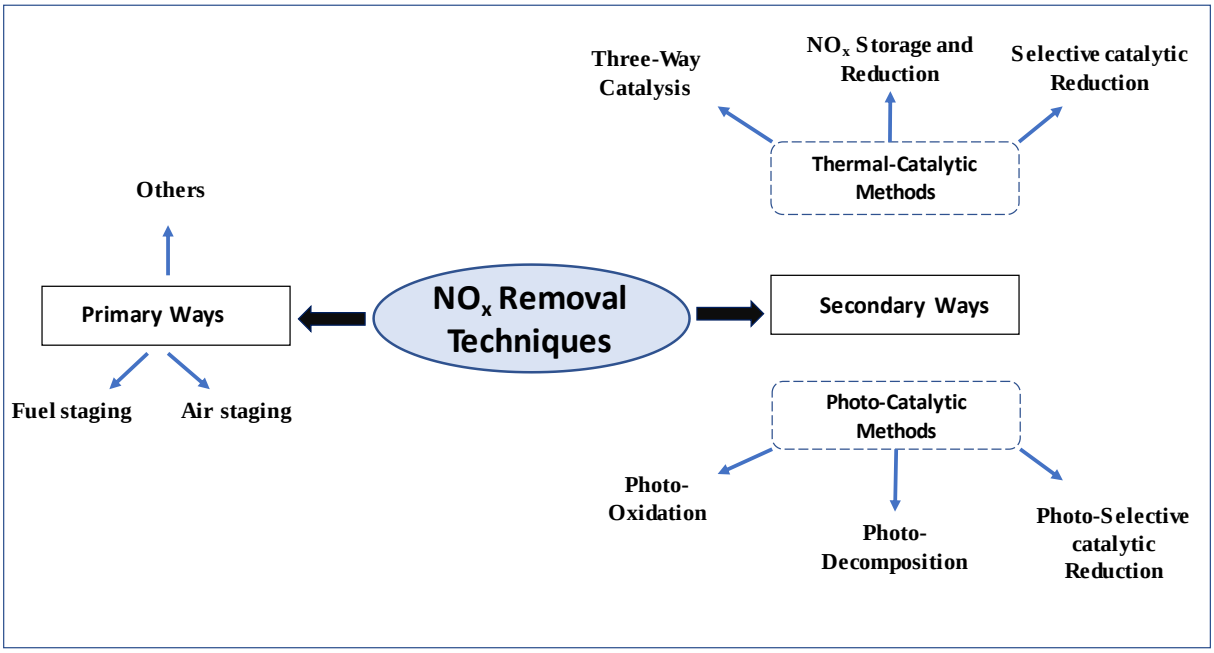

Figure 1.2: NO_x Removal Techniques Ref [17].

1.1.4.1 Thermal catalytic methods for NO_x Removal

NO_x abatement can be performed efficiently using thermal catalytic technologies at elevated temperatures (*e.g.* 200 - 550 ℃) with an intend to curtail the toxic NO_x emissions at the source of generation [18]. Three of the important secondary methods that use thermal catalytic technology for NO_x abatement may be described as follows:

- selective catalytic reduction/SCR
- NO_x storage and reduction/NSR
- three-way catalysis/TWC

Selective catalytic reduction (SCR) is one of the methods commonly used for NO_x control. Generally, SCR is performed with either ammonia (NH_3) or urea (NH_2-CO-NH_2) as a reducing agent in the presence of oxygen according to following reactions [19], [20]:

$$4NH_3 + 4NO + O_2 \rightarrow 4N_2 + 6H_2O \quad (15)$$

$$6NO + 4NH_3 \rightarrow 5N_2 + 6H_2O \quad (16)$$

$$6NO_2 + 8NH_3 \rightarrow 7N_2 + 12H_2O \quad (17)$$

$$2NO_2 + 4NH_3 + O_2 \rightarrow 3N_2 + 6H_2O \quad (18)$$

The optimum temperature range for the reaction varies between 200-550 °C according to the catalyst used. The intense use of NH_3 can cause undesirable species to form which may lead to catalyst poisoning and deactivation [17].

NO_x storage and reduction (NSR) also known as the Lean NO_x Trap (LNT), is another heterogeneous catalytic approach that was first developed by Toyota in 1994 [21], [22]. This method operates in cycles where, NO is continuously oxidized into NO_2 over a catalyst (*i.e.* precious metal such as Pt, Pd or Rh). Subsequently the generated NO_2 is captured on a basic oxide (*e.g.* BaO) in the nitrate form (NO_3^-). A reductant is fed to the exhaust that desorbs and reduces the stored NO_x to regenerate catalyst for the next period [23]–[25]. An important limitation of using NSR method is the sulfur poisoning which occurs by the interaction of SO_x with BaO and alumina to yield sulfates that block several storage sites for further adsorption of nitrates. [26]. The three-way catalysts (TWC) is another method for NO_x control, emitted from gasoline engines which employs noble metals such as platinum or rhodium, supported on a high surface area oxide, and an oxygen storage component [27]. Thermal catalytic De*NO*$_x$ technologies need to be operated at elevated temperatures at the source of generation. A major challenge is the reduction of gaseous NO_x species after their point of origin under ambient conditions (*i.e.* at room temperature and under atmospheric pressure).

1.1.4.2 Photocatalytic methods for NO_x removal

Photocatalysis is another technology which uses solar energy to remove undesirable NO in an economically sensible and environmentally friendly way. Photocatalytic NO_x removal can be categorized into three approaches: photo-decomposition, photo- SCR and photo-oxidation [17]. Photo- decomposition and photo-SCR are based on the chemical reduction methods. Therefore, conversion of NO into N_2 and other harmless compounds is desired. On the other hand, the main aim in photo-oxidation is to transform NO_x species into surface nitrate and nitrite species using a semiconductor material possessing a suitable band structure that can be activated by sun light.

1.1.4.2.1 Photocatalytic NO_x Oxidation and Storage (PHONOS)

Photocatalytic NO_x Oxidation and storage (PHONOS) is a De*NO*$_x$ technique that can store airborne NO_x in the solid state under ambient conditions after the point of NO_x emission to the atmosphere [28]–[31]. The aim of this approach is converting NO_x species into surface nitrate and nitrite using a semiconductor material, solar energy, water and atmospheric oxygen [32]. In this methodology, photocatalysts based on titanium dioxide (TiO_2), has been widely utilized to combat urban NO_x pollution [33]. The mechanism for the photocatalytic oxidation of NO on TiO_2 proceeds through multiple pathways which yield nitrites and/or nitrates on the catalyst surface [34]–[36]. NO photooxidation on TiO_2 starts when a photon with sufficient energy is absorbed by TiO_2, which leads to promotion of electrons from valance to conduction band and consequent formation of electron and hole (*i.e.* e^- - h^+) charge carriers and proceeds with the trapping of these charge carriers to form various surface species (reactions 19-21). As demonstrated in Figure 1.3, the generated holes oxidize water molecules to form hydroxyl radicals and electrons in the conduction band can reduce oxygen in the air and lead the formation of superoxide anions [37]. NO on the TiO_2 surface is photo-oxidized via its

interaction with surface hydroxyl radicals ($^{\bullet}OH_{ads}$) or holes (h^+) forming HNO_2 and NO_2 as by-products, finally yielding HNO_3 by the attack of hydroxyl radicals or holes [38].

$$TiO_2 + h\nu \longrightarrow TiO_2\ (h^+ + e^-) \quad (19)$$

$$TiO_2\ (h^+) + H_2O_{ads} \longrightarrow TiO_2 + {}^{\bullet}OH_{ads} + H^+ \quad (20)$$

$$TiO_2\ (e^-) + O_{2ads} \longrightarrow TiO_2 + O_2^{\bullet -}{}_{ads} \quad (21)$$

$$NO_{ads} + {}^{\bullet}OH_{ads} \longrightarrow HNO_{2ads} \quad (22)$$

$$HNO_{2ads} + {}^{\bullet}OH_{ads} \longrightarrow NO_{2ads} + H_2O \quad (23)$$

$$NO_{2ads} + {}^{\bullet}OH_{ads} \longrightarrow HNO_{3\,ads} \quad (20)$$

$$TiO_2\ (h^+) + NO_{ads} + H_2O_{ads} \longrightarrow HNO_{2ads} + H^+ \quad (21)$$

$$TiO_2\ (h^+) + HNO_{2\,ads} \longrightarrow NO_{2\,ads} + H^+ \quad (22)$$

$$TiO_2\ (h^+) + NO_{2\,ads} + H_2O_{ads} \longrightarrow HNO_{3\,ads} + H^+ \quad (23)$$

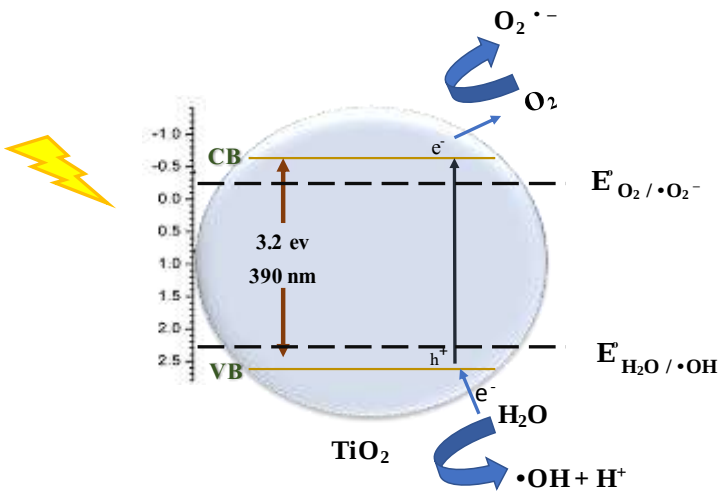

Figure 1.3: General mechanism of photocatalysis on TiO_2.

In another mechanism [39], [40], NO oxidation can occur either *via* superoxide anions (reactions 28-29) or *via* an electron deficient surface oxygen species (reactions 30-32). It is crucial to emphasize that adsorbed water plays an important role in the photocatalytic oxidation of NO, as indicated in reactions 19-32.

$$NO_{ads} \xrightarrow[H^+]{O_2^{\bullet -}{}_{ads}} \begin{cases} \rightarrow NO_{2ads} + {}^{\bullet}OH & (28) \\ \rightarrow HNO_{3ads} & (29) \end{cases}$$

$$TiO_2(h^+) + TiO_2(O_s) \longrightarrow TiO_2(O_s^{\bullet}) \quad (30)$$

$$NO_{ads} \xrightarrow{TiO_2(O_s^{\bullet})} NO_{2ads} + TiO_2(V) \xrightarrow{H_2O} TiO_2 + 2H^+ \quad (31)$$

$$NO_{2ads} \xrightarrow[H_2O]{TiO_2(O_s^{\bullet})} TiO_2 + NO_3^-{}_{ads} + 2H^+ \quad (32)$$

1.2 Titanium Dioxide

TiO_2 in various forms and types has revealed great potential for photocatalytic oxidation of harmful species both for gas and liquid phases due to its chemical and thermal stability, nontoxicity, cost effectiveness and availability. Photocatalytic performance of TiO_2 is strongly influenced by the particle size, degree of crystallinity and morphology. It is well known that titania has three main polymorphs in nature under normal atmospheric pressures: anatase, rutile and brookite. Rutile is the most stable form of titanium dioxide while anatase and brookite both are metastable phases and with calcination at high temperatures exceeding 600°C, they transform into the thermodynamically stable rutile polymorph [41][42]. Because brookite is difficult to be synthesized, it is rarely reported as a photocatalyst and mainly anatase and rutile are used in the photocatalytic applications of TiO_2. Besides, other high-pressure phases of TiO_2

are also reported in the literature [43] such as TiO_2 (II) with the alpha-PbO_2 structure, TiO_2 (B), TiO_2 (H), baddeleyite phase, fluorite phase and pyrite phase. The stability of these phases has been studied in several publications However, these are of minor importance for research and development applications due to their limited stabilities under ambient conditions [43].

Crystal structure along with some fundamental properties for the three main titania polymorphs are summarized in Table 1.2.

Table 1.2: Some properties of anatase, rutile and brookite. Adapted from Ref [43].

	Anatase	**Rutile**	**Brookite**
Unit cell	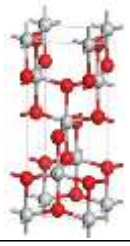		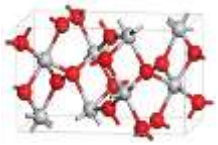
Crystal structure	**Tetragonal**	**Tetragonal**	**Rhombohedral**
Atoms per unit cell	**4**	**2**	**8**
Lattice parameters (nm)	**a = b = 0.3785, c = 0.9514**	**a = b = 0.4594, c = 0.2959**	**a = c = 0.5436, b = 0.9166**
Crystal size (nm)	**<11**	**>35**	**11–35**
Bandgap (eV)	**3.21**	**3.0**	**3.13**

UV-UV-visible reflectance spectra for anatase, rutile and brookite polymorphs with corresponding bandgaps are shown in Figure 1.4.

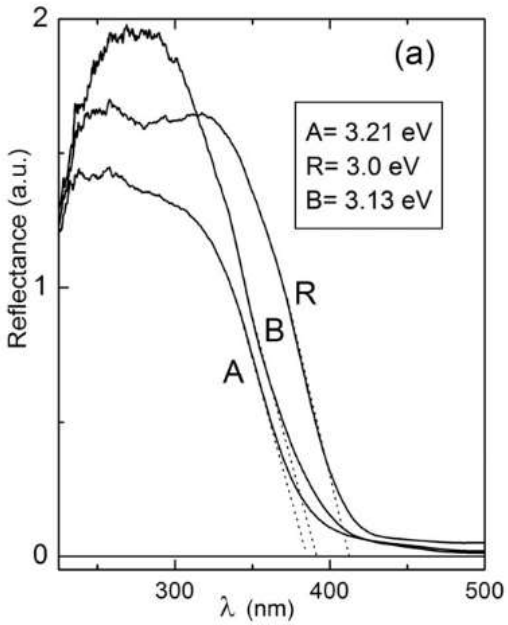

Figure 1.4: UV–visible reflectance spectra of for the phase-pure titania nanomaterials A: anatase, R: rutile and B: brookite. Adapted from Ref [44].

Another parameter on which the photocatalytic efficiency of TiO_2 is strongly dependent is the electron-hole recombination. While ability of anatase to absorb solar light is lower than rutile considering the greater band gap for anatase (3.2 eV) than rutile (3.0 eV), photocatalytic activity of anatase is claimed to be better than rutile [41]. This is due to the higher surface coverage of hydroxyl radicals, smaller grain size, and most importantly slower charge carrier (electron-hole pair) recombination rate of anatase (0.2 ns) compared to rutile phase (5.0 ns) [45]. Figure 1.5.a displays direct recombination of photogenerated electrons from conduction to valance band of rutile. Indirect bandgap of anatase shown in Figure 1.5.b, prohibits direct recombination of electron-hole pairs, extending the life- time of photogenerated excitons compared to direct bandgap rutile [44].

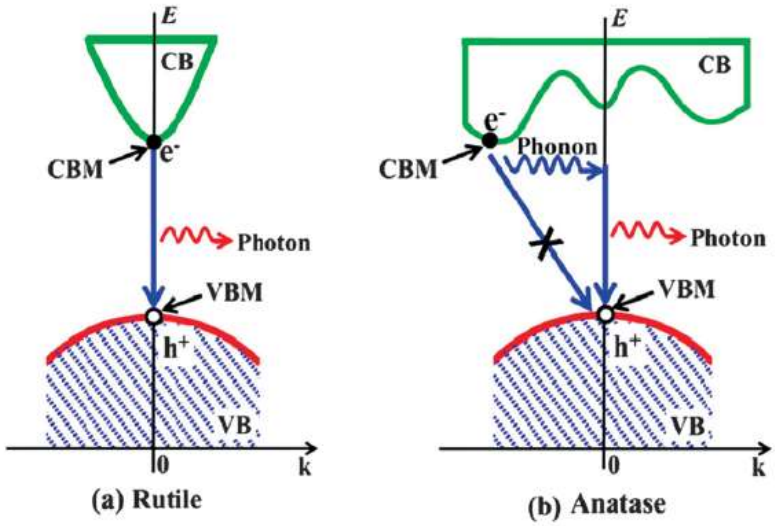

Figure 1.5: Recombination process of photogenerated electron-hole for a) direct bandgap rutile. b) indirect bandgap anatase. Adapted from Ref [41].

Despite its advantages, large bandgap of TiO_2 (3.2 eV corresponding to a wavelength of ~ 390 nm, allowing the harvesting of only UV-A light), high recombination rate and low selectivity towards NO_x storage necessitate the improvement of the photocatalytic efficiency of TiO_2 [18]. For this purpose, different strategies have been employed such as metal [46], non-metal doping [47], surface modification with polymers [48] and use of QDs for TiO_2 functionalization [29]. In the current study, colloidal quantum well nanoplatelets were introduced to TiO_2 in an attempt to enhance photocatalytic efficiency. Semiconductor NPL provide novel opportunities in photocatalytic applications as their thicknesses, diameters, shapes, electronic and optical properties can be fine-tuned with high precision via colloidal synthesis and hetero-structure growth strategies. In addition, 2D semiconductor NPL can also be utilized to enhance light absorption/harvesting and photon-induced charge (electron and/or hole) transfer properties of the overall photocatalytic system. They can be more advantageous as compared to conventional quantum dot (QD) systems due to the stronger light absorbance capability of NPL, which can be attributed to the NPL's extraordinary large absorption cross-

section per particle, associated with their very tight quantum confinement and the relatively larger volume compared to QD systems[49].

1.3 Quantum Confinement Effect

The quantum confinement effect is observed when the size of the particle is sufficiently small to be comparable to electron wavelength. It is the spatial confinement of electron-hole pairs in one or more dimensions within a material. Due to confinement of electronic wave function to the physical dimensions of particles, electronic energy levels become discrete and loss continuous like feature(*i.e.* as in bulk form) [50], [51]. A quantum confined structure can be classified in three groups depending on the confinement orientation/configuration, i) 2D-quantum-wells (are confined in one dimension), ii) 1D-quantum-wires (are confined in two dimensions), and iii) 0D- quantum-dots (are confined in 3 dimensions). Figure 1.6 displays quantum confinement and subsequent density of electronic states (DOS) for 3D, 2D, 1D and 0D structures in which Y axis stands for energy and X axis represents density of states. For a bulk semiconductor with continuous energy levels, electrons and hole are free to move in all directions without any confinement. However, in quantum wells charge carriers are confined to move in a plane and are free to move in two dimensions, , in quantum wires they can move only in one direction and in quantum dots charge carriers are confined in all three dimensions.

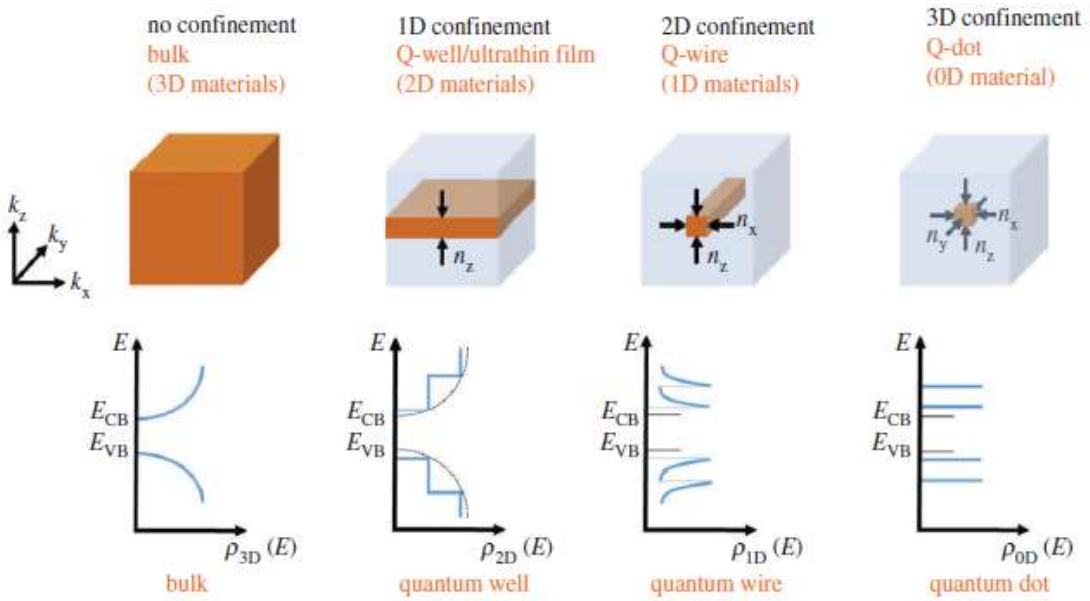

Figure 1.6: Electronic density od states for semiconductors as a function of dimensions. Adapted from Ref [50].

1.4 Quantum well nanoplatelets

Colloidal quantum wells (CQW), also known as nanoplatelets (NPL) constitute a class of colloidal semiconductor materials with atomically precise thicknesses governing their electronic structure [52]. In a quantum well, excitons are restricted to move only in two dimensions, where they are free to move in lateral directions but feel a strong confinement in the orthogonal thickness direction.

Quantum well NPL heterostructures with various chemical compositions and vertical thicknesses reveal different optical properties. Also, some studies show that optoelectronic properties of NPL can be enhanced by covering a nanocrystal with a shell or crown of another semiconductor. Therefore, in addition to core-only structures [53], different architectures such as core/crown (laterally grown shell) [54], core/shell (vertically grown shell) [55], and core/crown/shell [56] structures can also be synthesized. Schematic representation of these structures is shown in Figure 1.7.

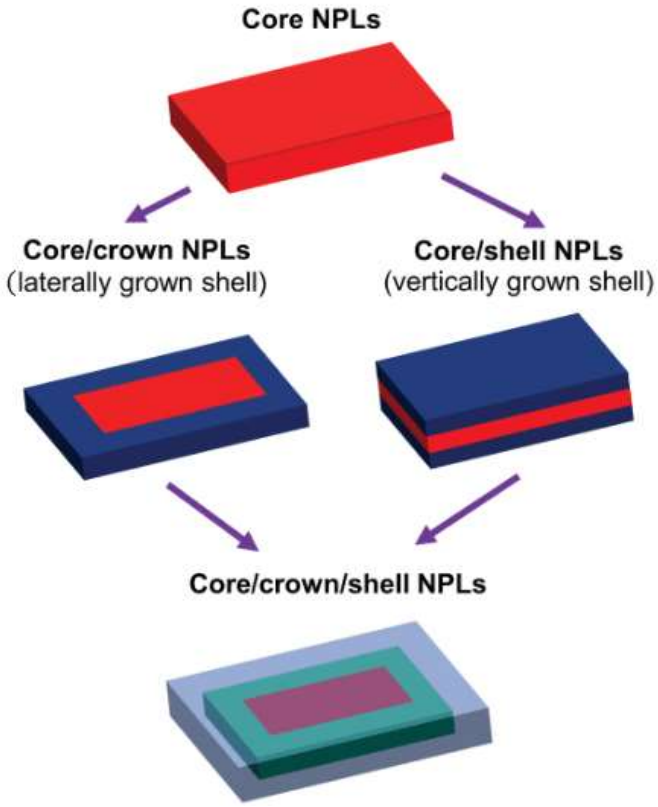

Figure 1.7: Schematic representation of different configurations in NPL. Adapted from Ref [57].

1.4.1 Core/Shell NPLs

Core/shell NPL are formed by coating the core NPL with a different type of semiconductor from top and bottom surfaces. The growth of the shell was first reported by Talapin [58] and Mahler [55] *via* growth of CdS shells on seed CdSe NPL at room temperature using the colloidal atomic layer deposition technique. With this method, using a Xe lamp (λ = 400 nm), 80% of quantum yield (QY) was achieved. However, precise control of optical properties was not accomplished by this technique. With the growth of a CdS shell on CdSe NPL, FWHM of PL peak increased from 37 to 65 meV due to electron-phonon coupling with the addition of the shell [57]. High-temperature shell-growth was also reported by Norris *et al.* [57] which was based on the addition of low reactivity precursors at ~ 300 °C. Several heating cycles through

the growth of CdS shell yielded high QY along with narrow emission and improved thermal stability of core/shell NPL making them excellent candidates for LED applications [59]. The absorption spectrum of core/shell NPL in Figure 1.8.a shows a red shift of approximately 120 nm with the growth of shell, which is due to electronic delocalization of charge carriers through the entire thickness of the platelets.

1.4.2 Core/Crown NPLs

The first core/crown heterostructures were obtained by Artemyev in 2013 *via* lateral growth of CdS crown on seed CdSe NPL [60]. The crown can be grown in lateral direction while maintaining thickness, so that both core and crown with the same thickness can contribute to the absorption of illuminated photons which in turn, leads to an increase in absorption cross section per particle. Unlike the core/shell NPL, in these heterostructures, no shift to higher wavelength in absorption can be observed (Figure 1.8.b) due to the insignificant change in the confinement of the carriers in the lateral dimension compared to thickness with the addition of the crown [56], [61].

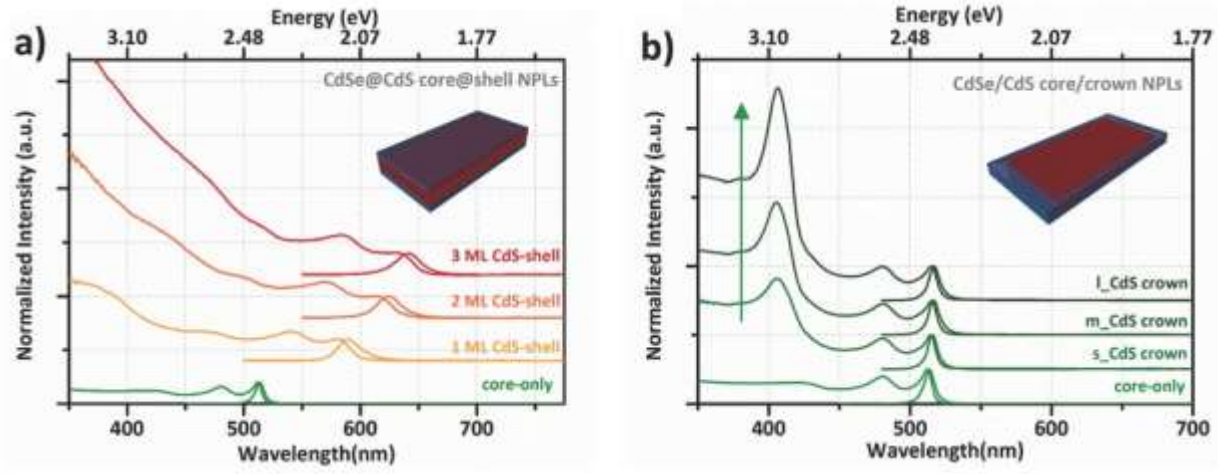

Figure 1.8: Absorption spectra of a) core/shell NPLs, b) core/crown NPL. Adapted from Ref [56].

Depending on the band alignment (*i.e.* position of the valance and conduction bands) of core and crown and subsequent bandgap energy, different heterostructures can be obtained with type-I, type II or quasi type-II nature [62]. Energy diagrams for these structures are given in Figure 1.9.

In type-I electronic structures, a crown with wider bandgap is used to cover the narrow bandgap core. On the other hand, a narrow-bandgap crown semiconductor and a wide-bandgap core leads the formation of inverse type-I material. In both configurations, both charge carriers' wave functions are confined in the same part of the structure [63]. In type-II band structure, the bandgap energies of core and crown semiconductor are comparable and the band edges are shifted with respect to each other so that, the valance or conduction band of core is placed within the bandgap of the crown. Unlike type-I NPL, in type-II heterostructures, electron and hole wave functions are localized in different parts of the structure (due to having specific band alignment) resulting in additional separation of charge carriers yielding a long lifetime of photoexcited electron-hole pairs. Type-II band alignment can be achieved by the combination of materials such as CdSe/CdSeTe [64], [65]. Partial separation of electron and hole occurs in quasi type-II band alignment and it allows delocalization of electron wave function over the entire structure. It is worth noting that, these systems are extremely sensitive to quantum confinement effects and changing the relative size of the core and/or the crown causes transitions from quasi type II to type I or II regimes [65]. The choice of core and crown semiconductor materials should be in a way to prevent the formation of defects at the interfaces which can be achieved by using similar structures and lattice parameters in the material design.

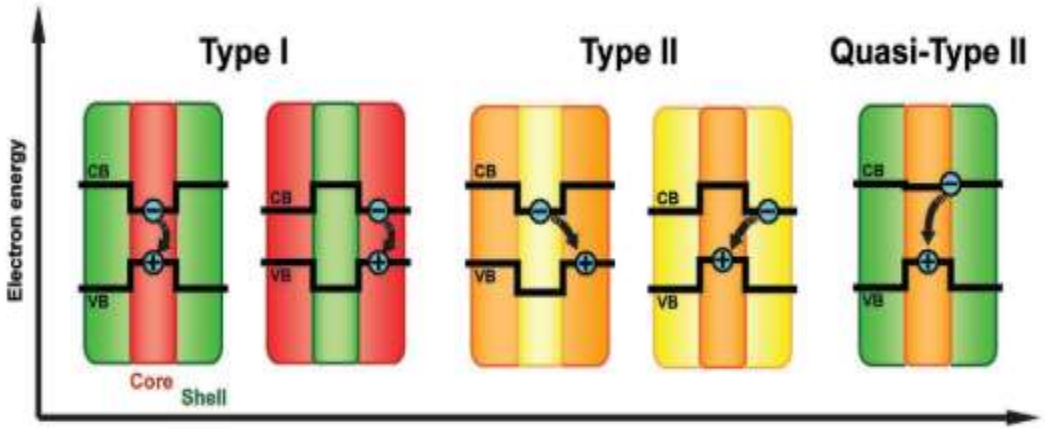

Figure 1.9: Schematic representation of energy structures for core/shell- core/crown heterojunctions. Adapted from Ref [62].

1.5 Scope of The Study

The main focus of this study is to design a visible responsive photocatalyst in order to improve photocatalytic activity of TiO_2 in Photocatalytic NO_x Oxidation and Storage applications (PHONOS). Commercially available benchmark Degussa P25 is used as the titanium dioxide source. Degussa P25 is composed of 75% anatase, 15% rutile and 10% of amorphous titania and it was reported that P25 revealed better photocatalytic activity in numerous reactions compared to many other forms/polymorphs of pure titania [66]. However, its wide bandgap only allows its utilization under UV light.

In this study, core/crown nanoplatelets were used in attempt to modify TiO_2 to achieve better photocatalytic activity with an increase in selectivity towards NO_x storage. Oleic acid capped CdSe/CdSeTe core/crown NPL with type II band alignment were selected since in these NPL, photo-excited electrons are expected to be localized in the CdSe core, while holes may be trapped in the CdSeTe crown, forming indirect excitons with presumably much longer

lifetimes [64], [67], [68]. Also, NPL with large absorption cross-section are capable of harvesting a greater portion of sunlight. Furthermore, presence of NPL create additional sites for NO_2 adsorption which consequently improves selectivity towards NO_x storage. The main aim of incorporation of NPL can be summarized in Figure 1.10. As demonstrated in Figure 1.10, conduction band of TiO_2 lies below the conduction band of CdSe core, therefore overall photo-generated electrons will be trapped in TiO_2 's conduction band, while generated holes will be confined in CdSeTe crown since CdSeTe has a higher valance band. This efficient separation of electrons and holes would decrease the recombination rate leading to improved PHONOS performance.

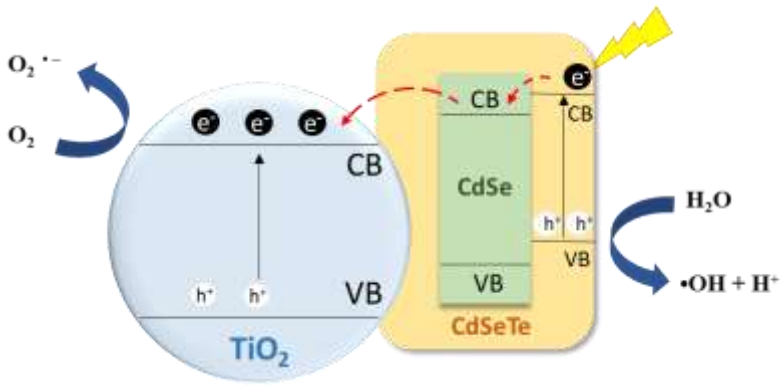

Figure 1.10: A possible illustration of electron-hole transport in CdSe/CdSeTe/P25 catalyst.

Figure 1.11 illustrates overall PHONOS process on the NPL/P25 catalyst. Atmospheric NO_x oxidation occurs in the presence oxygen, water and an excitation source and the gaseous NO_x oxidation products are trapped on catalyst surface as nitrates/nitrites.

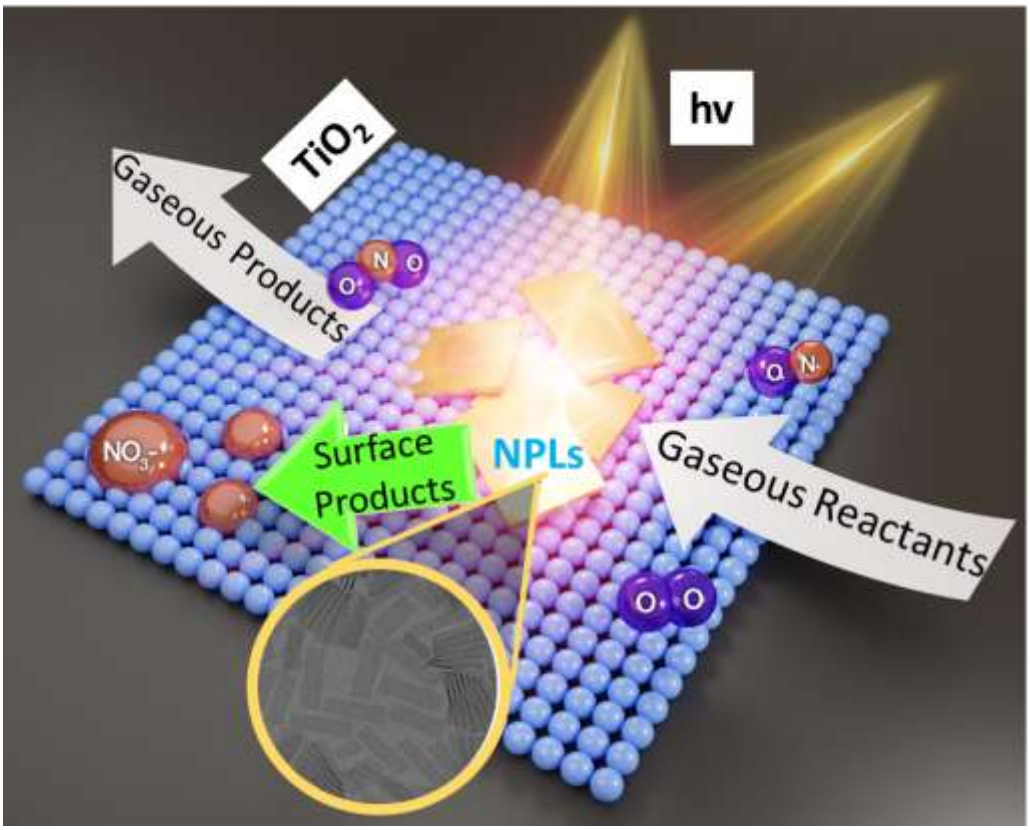

Figure 1.11: Overall PHONOS process on NPL/P25.

The toxicity and cost of the photocatalyst material are important factors and the incorporation of CdSe/CdSeTe NPL are neither cost efficient nor environmentally friendly. Nonetheless, is shown for the first time that photocatalytic NO oxidation performance of titania surfaces can be significantly boosted via 2D quantum-wells (i.e. CdSe/CdSeTe nanoplatelets/NPL). Thus, the current study pave the way for future studies where the photocatalytic performance of titania (as well as other semiconductors) not only in NO oxidation but presumably in many other photo-oxidation reactions can be fine-tuned and enhanced by designing a non-toxic new quantum-well architectures with controlled electronic structures.

2 Experimental

2.1 Sample preparation

Preparation of CdSe/CdSeTe/P25 composites were achieved by using the synthesized CdSe/CdSeTe quantum well nanoplatelets (see Appendix) and incorporating them onto P25. List of the used chemicals for the synthesis is given Table 2.1. Utilized chemicals were purchased from Sigma Aldrich and used as received without further purification.

Table 2.1 List of used chemicals in synthesis part

Chemical name	
Cadmium nitrate tetrahydrate	$Cd(NO_3)_2.4H_2O$; 99% trace metal basis
Cadmium acetate dihydrate	$Cd(OAc)_2.2H_2O$; 98%
Sodium myristate	$CH_3(CH_2)_{12}COONa$, ≥99%
Titanium (IV) oxide	P25, ≥99.5% trace metal basis
1-Octadecene	ODE, technical grade
Selenium	(Se), 99.99% trace metals basis
Tellurium	(Te), 99.99% trace metals basis
Oleic acid	OA, 90% technical grade
Trioctylphoshine	TOP, Sigma Aldrich

2.1.1 Preparation of CdSe/$CdSe_{0.75}Te_{0.25}$/P25 composite Materials

Commercially available Degussa P25 is used as titanium dioxide source as a photocatalyst. To synthesize CdSe/$CdSe_{0.75}Te_{0.25}$/P25 composite systems, different volumes of CdSe/$CdSe_{0.75}Te_{0.25}$ NPL colloidal suspensions in toluene were drop-cast on 250 mg of P25 (*i.e.* TiO_2) in a petri dish. After physical mixing of the NPLs with P25 for 2 min, samples were dried in an oven at 70 °C for 18 h. The samples were labeled as *X*NPL/P25 (*X*=0.1, 0.5, 1.0, 2.0, and 6.0). Furthermore, additional samples were also prepared, in order to elucidate the effect of toluene (*i.e.* NPL dispersing medium) on the photocatalytic performance of P25. For this purpose, various amounts of toluene were drop-cast on P25 at RT followed by evaporation and drying at 70 °C for 18 h. These samples are designated as *X*T/P25, where *X* represents the volume of toluene dosed on P25 in mL (*i.e.* *X* = 0.1, 0.5, or 2.0 mL). Names of these samples along with abbreviation names are listed in Table 2.2.

Table 2.2: List of prepared samples

Sample name	**TiO_2 (Degussa P25) amount (mg)**	**CdSe/CdSeTe NPL amount (ml)**	**Toluene amount (ml)**
0.05 NPL/P25	250	0.05	-
0.1 NPL/P25	250	0.1	-
0.5 NPL/P25	250	0. 5	-
1.0 NPL/P25	250	1	-
2.0 NPL/P25	250	2	-
6.0 NPL/P25	250	6	-
0.1 T/P25	250	-	0.1
0.5 T/P25	250	-	0.5
2.0 T/P25	250	-	2

2.2 Photocatalytic Activity Measurements

2.2.1 Flow Reactor Setup for Photocatalytic NO_x Oxidation and Storage (PHONOS)

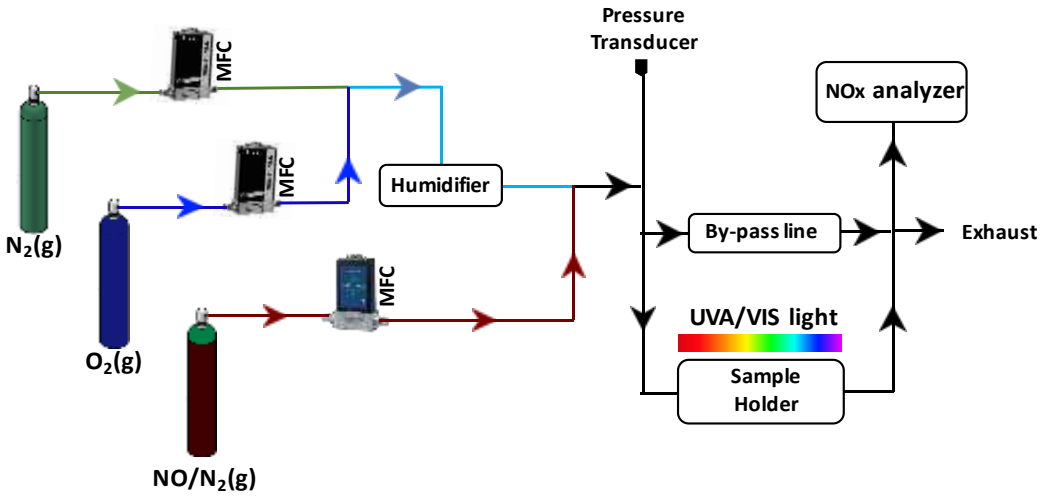

Figure 2.1: Schematic representation of custom-made photocatalytic NO_x Oxidation flow rector system Ref [18].

The photocatalytic NO_x oxidation and storage measurements were conducted at room temperature using a custom-designed flow reactor demonstrated in Figure 2.1. The flow reactor consists of three gas lines that are made of 1⁄4-inch Swagelok stainless steel tubing and Swagelok nupro VCR valves which are connected to gas tanks including N_2 -99.99%, O_2 - 99.00%, NO - 100 ppm balanced with N_2. The volumetric flow rates were set to be 0.750 SLM (standard liters per minute) for N_2(g), 0.250 SLM for O_2(g), and 0.010 SLM for NO(g). Mass flow controllers (MFCs) were utilized to control the gas flow rates with high accuracy and each MFC (MKS1479 A for N_2(g) and O_2(g), and Teledyne HFC-202 for NO(g) diluted in N_2(g)) was calibrated specifically for each type of gas flowing through it. Total gas flow rate over the

photocatalyst was kept at 1.01 SLM ± 0.05 SLM, where the NO(g) content of the inlet gas mixture was fixed at 1.00 ppm. The pressure inside the reactor was maintained at *ca*. 1 bar and measured with an MKS Baratron 622B capacitance manometer. Humidity level of the gas mixture was also controlled by dosing varying amounts of water vapor into the inlet gas mixture (*i.e*. before the reactor entrance) with the help of a PermSelect (PDMSXA-2500) semipermeable membrane module attached to an external variable-temperature water chiller/recycler. The mixture of artificially polluted air was fed to the photocatalytic reaction chamber and passed over the photocatalyst. The changes in NO_x, NO and NO_2 outlet concentrations were monitored using a chemiluminescent NO_x analyzer, Horiba APNA-370 with a 0.1 ppb sensitivity and 1 Hz detection speed according to HORIBA APNA manual. APNA-370 is an ambient nitrogen oxide monitor using the chemiluminescence method as its operating principle. This monitor provides to continuously measure the concentrations of nitrogen oxides (NO, NO_2, and NO_x (NO + NO_2)) in the atmosphere. The working principle of chemiluminescence analyzer is based on the reaction of NO with ozone [69]. When O_3 is introduced to the sample gas mixture containing NO using an ozonizer unit, a portion of NO in the sample gas is oxidized to NO_2 and forms the excited state NO_2* according to reaction 33. Generated NO_2* emits light with a range of wavelength between 600-3000 nm centered about 1200 nm and relaxes into its ground state. This phenomenon of light emission is called chemiluminescence as shown in reaction 34.

$$NO + O_3 \rightarrow NO_2^* + O_2 \quad (33)$$

$$NO_2^* \rightarrow NO_2 + hv \quad (24)$$

Reaction 33 is extremely fast (a few nanoseconds). It involves only NO and is mostly unaffected by the coexistence of other gases. When the NO concentration is low (*i.e*. 0-10 ppm), the light intensity is linearly proportional to the NO concentration. In APNA-370, the

analyte gas is divided into two separate detection chambers. The first detection chamber is used for the direct measurement of the NO concentration in the NO_x analyte mixture (*i.e.* [NO]) as shown in reactions 33 and 34. The second detection chamber is for the measurement of the NO_2 concentration (*i.e.* [NO_2]). In the second detection chamber, NO_2 in the NO_x analyte mixture is reduced to NO via a tungsten-based heterogeneous catalyst and then this particular analyte sample containing additional NO obtained from NO_2 reduction is sent back to the first chamber for the analysis of the total [NO] coming from the 2nd chamber. Then by subtracting the [NO] concentrations obtained from the second chamber from the first chamber yields [NO_2]. Furthermore, total NO_x concentration in the exhaust line can also calculated using [NO] and [NO_2], where [NO_x(total)] ≡ [NO] + [NO_2)]. Note that in the presence of O_2 (g) and H_2O(g) (*i.e.* under oxidizing reaction conditions) no additional NO_x products other than NO and NO_2 are expected to be present in the analyte gas sample. In other words, NO reduction products such as N_2 or N_2O are not expected to exist in the analyte mixture.

In the NO_x analyzer, sample gases are switched to the NO_x, NO, and reference gas lines every 0.5 s with solenoid valves and are introduced to the reaction chambers in a subsequent manner. On the other hand, the ambient air is separately sucked through the air filter, dried by a self- reproducing-type silica gel dryer, and used to form ozone in the ozonizer unit.

In the photocatalytic PHONOS measurements carried out in the current work, two different light sources were used. For the experiments performed with UV-A irradiation, an 8 W UV-A lamp (F8W/T5/BL350, Sylvania, Germany) was used, while for the experiments carried out with VIS light illumination, a 35 W metal halide lamp (HCI-TC 35 W/942 NDL PB 400−700 nm range, Osram) along with a commercial VIS transparent UV-A-blocker/filtering film (LLumar window film UV-A CL SR PS (clear)) was utilized in order to remove any contributions from UV-A photons during the VIS-light illumination. The incoming light flux

was measured before and after each UV-A and VIS-light measurements with a photoradiometer (HD2302.0, Delta Ohm/Italy) using a UV-A probe (315−400 nm) and a PAR VIS probe (400−700 nm), respectively. Typical VIS-light photon flux values used in the current experiments were within 450−500 μmol/(m^2 s), while typical UV-A-light power density values were within 7.7−8.3 W/m^2. It is important to note that the photon flux of the VIS light source was about 15 times greater than that of the UV-A light source. Relative percentile of VIS photon flux in typical solar radiation is 42% which is significantly greater than that of UV-A photon flux that contributes only 6% of incoming solar irradiation photon flux (The rest of solar irradiation is UV-B, UV-C and IR). Relative humidity and temperature of the reactor were measured using a Hanna HI 9565 humidity analyzer at the sample position in the photocatalytic flow reactor and these two parameters were kept within 50±3% at 23±2 °C during the photocatalytic tests, respectively. However, during VIS light experiments, reactor temperature reached up to 46 °C after a typical 60 min photocatalytic activity test due to the infrared photon emission form the VIS light source. Therefore, the effect of the increasing temperature was also studied additionally. For each photocatalytic activity measurement, 250 mg of photocatalyst was packed in a 2 mm × 40 mm × 40 mm polymethyl methacrylate (PMMA) sample holder shown in Figure 2.2 and placed into the flow reactor. Aged samples were exposed to UV-A or VIS irradiation source for 18 h at room temperature before the PHONOS performance test.

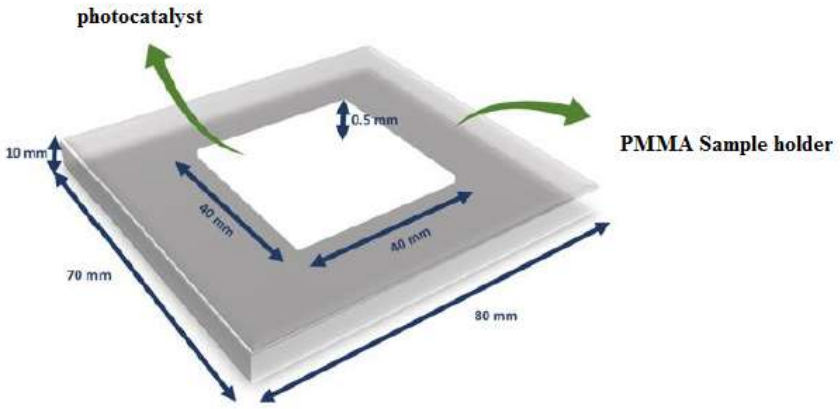

Figure 2.2: Illustration of the sample holders designed for photocatalytic performance tests.

A typical NO_x concentration profile during the PHONOS tests as a function of UV/VIS irradiation time is illustrated in Figure 2.3. The experiment started by feeding a synthetic polluted air gas mixture containing *ca.* 1 ppm NO(g) to the photocatalyst surface under dark conditions. During this initial step, also known as dark adsorption period, a slight decrease in the total NO and consequently NO_x concentration was observed due to adsorption of NO_x species on the reactor lines, expansion of the gas in the reactor as well as non-photocatalytic adsorption of NO_x on the photocatalyst surface. In addition, a tiny amount of NO_2(g) was produced due to thermal catalytic processes occurring on the catalyst surface. Following the saturation of the reactor system and photocatalyst surface after this induction period, NO_x(g) and NO(g) levels quickly returned to their original inlet values under dark conditions. In the next step, UV-A or VIS irradiation source was turned on which resulted in a drastic and long-term fall in NO(g) and total NO_x concentrations along with a small increase in the NO_2(g) level. Finally, after 1 h, when the experiment was completed, the light source was turned off and the concentrations returned to their initial inlet values.

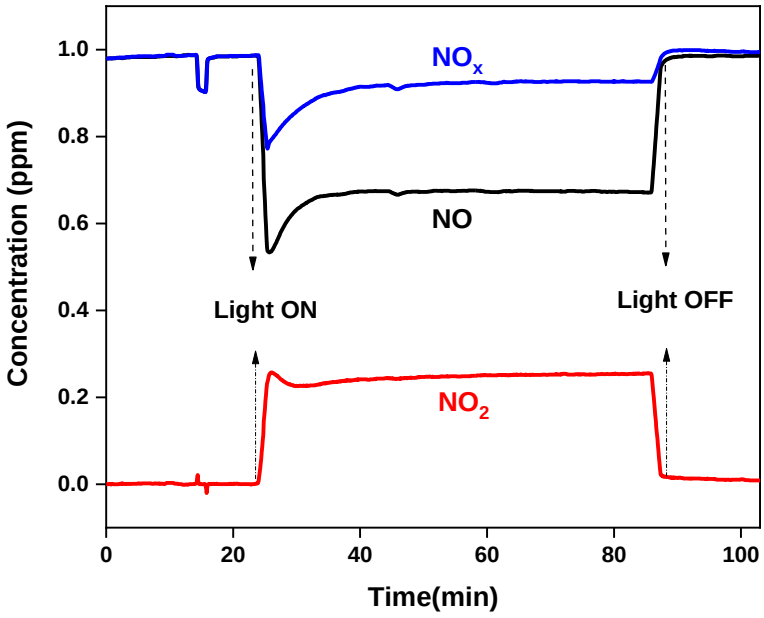

Figure 2.3: Schematic demonstration of a typical Concentration vs time profile recorded during Photocatalytic NO_x Oxidation and storage test.

2.2.2 Photocatalytic Performance Indicators

Different photocatalytic performance indicators (*i.e.* figures of merit) were defined to evaluate and quantify the relative photocatalytic activity of the samples by integrating the concentration versus time profiles, an example of which is given in Figure 2.4. %NO conversion, %selectivity, DeNO_x index and % photonic efficiencies are the variables that are used in this study to report photocatalytic NO_x Oxidation and Storage performance.

2.2.2.1 %NO Conversion and Selectivity

NO conversion represents total amount of NO gas that is photo oxidized into two main products: 1) NO can be photo oxidized to NO_2 which releases into atmosphere in the form of gaseous, or 2) it can be deposited in solid state in the form of nitrate / nitrite on the catalyst surface. It is an indication of the total oxidation activity of the photocatalyst. Consequently, one of the desirable outcomes for photocatalytic oxidation processes is to obtain high %NO

conversion values. NO conversion can be calculated using Equation 35 and are shown in purple bars in the histograms presented in the forthcoming figures.

$$\% \textbf{ NO Conversion} = \frac{\int([NO]_{in}-[NO]_{out})dt}{\int[NO]_{in}dt} x\ 100 \qquad (35)$$

The second parameter is called % Selectivity and is shown in Equation 36. % Selectivity is represented with green bars in the histograms given in the forthcoming figures. This term corresponds to the percentage of NO oxidation products that are stored on the catalyst surface in the solid state. Therefore, a high %Selectivity is a desirable catalytic property.

$$\% \textbf{ Selectivity } (towards\ NO_x\ Storage) = \frac{\int([NO_x]_{in}-[NO_x]_{out})dt}{\int([NO]_{in}-[NO]_{out})dt} x\ 100 \qquad (36)$$

In these calculations, it is assumed that NO (g) conversion is only due to the generation of gaseous NO_2 and/or formation of solid-state NO_x species. This is a reasonable assumption since NO_2 (g), HONO (ads), $HONO_2$ (ads) and NO_3^- (ads)/NO_2^- (ads) are the major products of the photocatalytic NO + O_2 reaction under the currently utilized reaction conditions [38].

2.2.2.2 DeNO_x Index

De*NOx* index is another performance parameter used in the current work to compare ultimate photocatalytic performance of the samples. According to Occupational Safety and Health Administration (OSHA), American Conference of Governmental Industrial Hygienists (ACGIH) and National Institute for Occupational Safety and Health (NIOSH); short term exposure limit value of NO is 25 ppm, whereas the corresponding limit value of NO_2 varies from 1 to 3 ppm. Therefore, based on above mentioned facts and the assumption that NO_2 contributes 3 times more than NO to total toxicity of the air, Bloh et al. established the De*NOx*

index parameter to assess the overall ultimate photocatalytic efficiency of the photocatalytic materials. In other words, De*NOx* index is a figure of merit that accounts for the net NO_x abatement effect of the photocatalyst by taking both NO conversion and NO_2 formation into consideration. If De*NOx* index has a positive value, it means that photocatalyst is reducing toxicity of the air by lowering the overall NO_x and is worth using that material for photocatalytic NOx oxidation-storage; otherwise it should not be used. The parameter defined in Equation (37) is a modified version of one proposed by Bloh and co-workers.

$$\textbf{De}\boldsymbol{NO_x}\textbf{ index} = \frac{\int([NO]_{in} - [NO]_{out})dt - 3\int([NO_2]_{out} - [NO_2]_{in})dt}{\int[NO]_{in}dt} \qquad (37)$$

2.2.2.3 Photonic Efficiency

It is important to note that, for a specific photocatalyst, *% NO* Conversion and % Selectivity values mentioned above vary with the incoming photon flux. Therefore, photocatalytic activity data can also be reported after normalization with the incident photon flux and calculation of the % Photonic Efficiency (*i.e.* % quantum yield) values as given in Equations 38 and 39 [70].

$$\textbf{NO}_\textbf{x}\textbf{ Storage \% Photonic Efficiency } (\xi) = \frac{n(NO_x\ stored\ on\ the\ catalyst\ surface)}{n(photon)}\ x\ 100 \qquad (38)$$

$$\textbf{NO}_\textbf{2}\textbf{ Release \% Photonic Efficiency } (\xi) = \frac{n(NO_2\ released\ to\ the\ atmosphere)}{n(photon)}\ x\ 100 \qquad (39)$$

where *n(photon)* is defined as:

$$n(photon) = \frac{(I\ x\ \lambda\ x\ A\ x\ t)}{(N_A\ x\ h\ x\ c)} \qquad (40)$$

In Equation 40, "*I*" represents the photon power density of the lamp; λ represents the mean emission wavelength of the lamp; "*A*" is the surface area of the photocatalyst exposed to light irradiation; *"t"* represents the duration of the performance test; "N_A" is the Avogadro's number; *"h"* is the Plank constant and *"c"* is the speed of light.

NO_x storage photonic efficiency and NO_2 release photonic efficiency % values described in Equations 38 and 39 denote the percentile of NO_x species stored in solid state and NO_2(g) molecules released to gas phase, respectively, per number of photons impinging on the catalyst surface during a 60 min-long photocatalytic activity test. Since the ultimate goal of the current work is to determine/compare/quantify the actual amounts of NO_x abatement under irradiation conditions similar to that of solar radiation, we will mostly focus on the % NO conversion and % Selectivity towards NO_x storage values in our discussion, however photonic efficiency values will also be discussed additionally where needed.

Figure 2.4 represents a hypothetical ideal photocatalyst which is both active and selective revealing high NO_x storage photonic efficiency, low NO_2 release photonic efficiency and a positive DeNO_x index value rendering itself a very favorable photocatalyst for the PHONOS process.

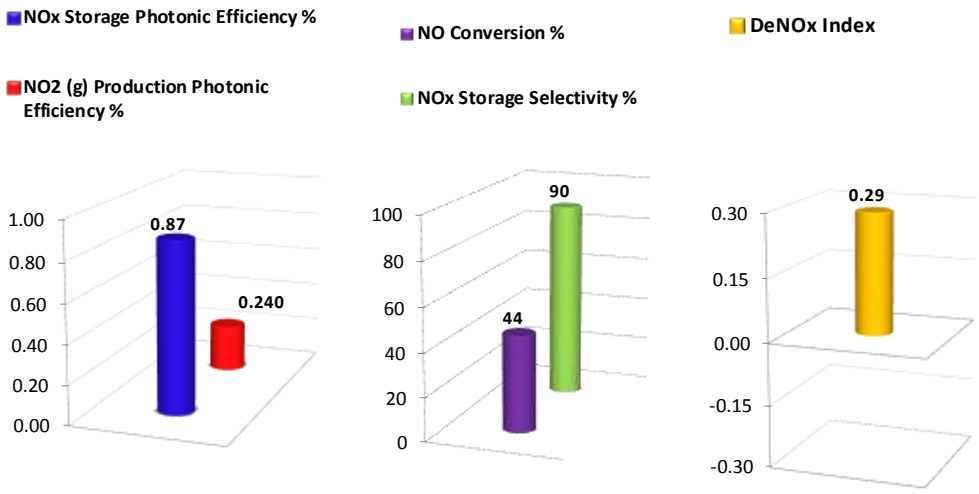

Figure 2.4: Photocatalytic performance parameters for a hypothetical ideal PHONOS photocatalyst.

2.2.3 Characterization Methods

Crystallographic structures of the synthesized materials were determined by using a PANalytical Empyrean XRD diffractometer equipped with Cu Kα irradiation source. (40 kv, 45 mA, λ=1.5405 Å). The powder samples were pressed into a silicon single crystal and placed in diffractometer to be scanned within 10-80° 2θ range with a scan rate of 0.04° S^{-1}. Transmission electron microscopy (TEM), scanning transmission electron microscopy (STEM), high angle annular dark field (HAADF) imaging and energy dispersive X-Ray (EDX) analysis experiments were carried out at 120 kV using a Hitachi HighTech HT7700 TEM equipped with BF-/DF-STEM-EDX modules at DAYTAM User Facility (Ataturk University, Erzurum, Turkey). X-ray photoelectron spectroscopy (XPS) experiments were performed with a SPECS PHOIBOS hemispherical energy analyzer. A monochromatic Al-Kα X-ray excitation source (15 kV, 400 W) was employed during the XPS data acquisition. BET specific surface area (SSA) measurements of the synthesized catalysts were determined by using nitrogen

adsorption–desorption isotherms obtained with a Micromeritics 3Flex surface area and pore size analyzer. Prior to SSA analysis, all samples were outgassed in vacuum for 2 h at 150 °C. Optical absorption properties of the samples were investigated *via* Diffuse Reflectance UV-A-VIS (DR-UV-A-VIS) Spectroscopy using a Cary 5000 UV-A-VIS-NIR Spectrometer equipped with a Varian Cary 2500 Internal Diffuse Reflectance (DR) Accessory. The photoluminescence (PL) spectra were obtained at room temperature using a Jobin-Yvon Horiba Fluorolog-3 spectrometer equipped with a 450 W ozone-free Osram XBO xenon arc lamp and a Hamamatsu R928 P detector. The excitation wavelength was 400 nm (*i.e.* 3.1 eV), which is well above the band gap of NPL. The fluorescence was monitored at a right angle relative to the excitation. Electron paramagnetic resonance (EPR) measurements were performed with a Bruker EMX Nano spectrometer with an integrated referencing for g-factor calculation using integrated spin counting units. The microwave frequency of the cavity was 9.41 GHz (X-band) and all spectra were measured at room temperature (RT) with 0.1 mT modulation amplitude, 2 mW microwave power and 120 scans (sweep time 60 s/scan, time constant 81.92 ms). Before the measurements, EPR samples were inserted into a spin-free 25 cm long quartz tubes (Qsil®, Germany). I*n-situ* EPR experiments were also carried out in the presence of UV-light irradiation using an ER 203 UV radiation system containing a short-arc mercury lamp (LSB 610 100W Hg, LOT-Quantum Design).

3 Results and Discussion

3.1 Characterization

3.1.1 Structural analysis by XRD

To analyze Crystal structures of core/crown CdSe/CdSeTe NPL, P25 (TiO_2), as well as CdSe/CdSeTe/P25 composites having different loadings of NPL, XRD measurements were carried out. X-ray diffraction patterns of CdSe/CdSeTe quantum well nanoplatelets are shown in Figure 3.1.a. XRD peaks at 2θ values of 12.83°, 19.71°, 38.03° and 49.81° are assigned to (111), (200), (220) and (311) facets of the CdSe core of NPL with a zinc blend structure . It is observed that, addition of a CdSeTe crown to the CdSe core does not lead to major changes in the XRD pattern of the CdSe core and initial crystal structure of CdSe core is preserved [65]. XRD profile of P25 in Figure 3.1.b demonstrates characteristic diffraction signals of TiO_2, indicating the existence of anatase (ICDD card no. 00-021-1272) and rutile (ICDD card no. 00-021-1276) domains. On the other hand, it can be interpreted from XRD patterns of P25 that, anatase is the dominant phase in P25. In terms of CdSe/CdSeTe/P25 samples, it is observed that incorporation of different loadings of quantum well nanoplatelets to P25 does not lead to any change in XRD pattern of CdSe/CdSeTe/P25 composites due to the very small loadings of NPL used in the functionalization of P25 and the small NPL particle sizes. Currently used minute loadings of CdSe/CdSeTe NPL were chosen to minimize the cost and toxicity of the photocatalyst.

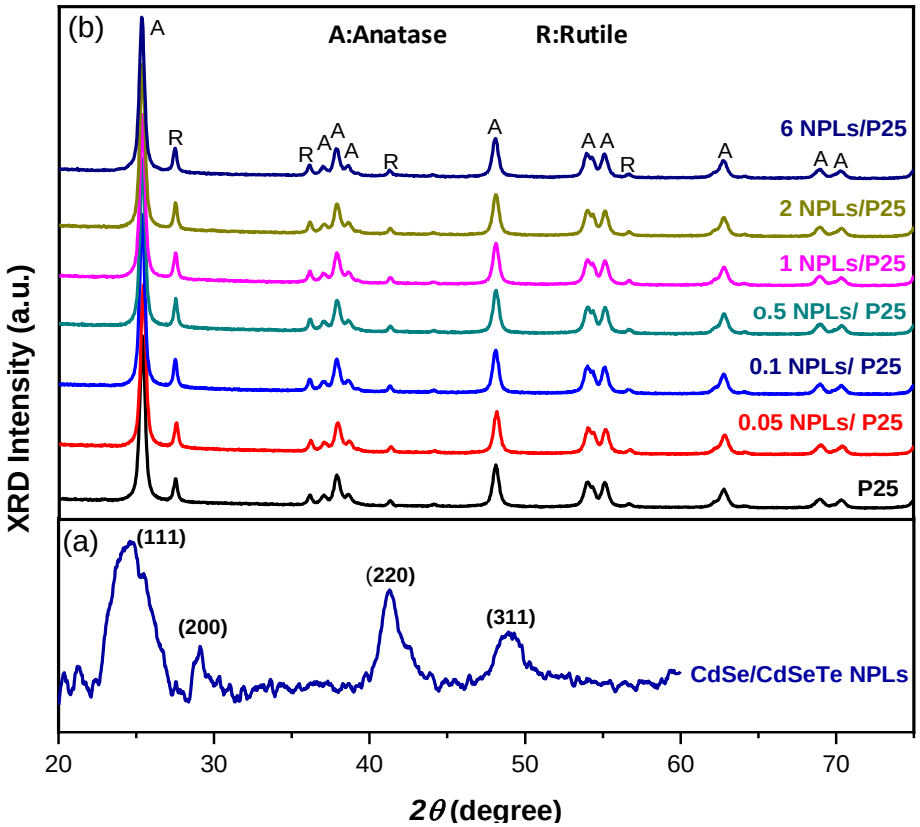

Figure 3.1: XRD diffraction patterns of a) CdSe/CdSeTe NPL (without TiO_2) and b) pure P25 and CdSe/CdSeTe/P25 composite materials with various NPL loadings.

3.1.2 Electron microscopy analysis via TEM

Figure 3.2 demonstrates several TEM images of CdSe/CdSeTe core/crown NPL in the absence of P25. Highly monodisperse and uniform 4 ML-thick NPL with a rectangular shape are visible in the TEM images. These rectangular NPL have sharp and well-defined rims exhibiting lateral dimensions of 90 nm × 30 nm. The stacks of NPL in these images affirm the excellent uniformity of these quasi-2D nanostructures both in terms of lateral dimensions as well as thickness.

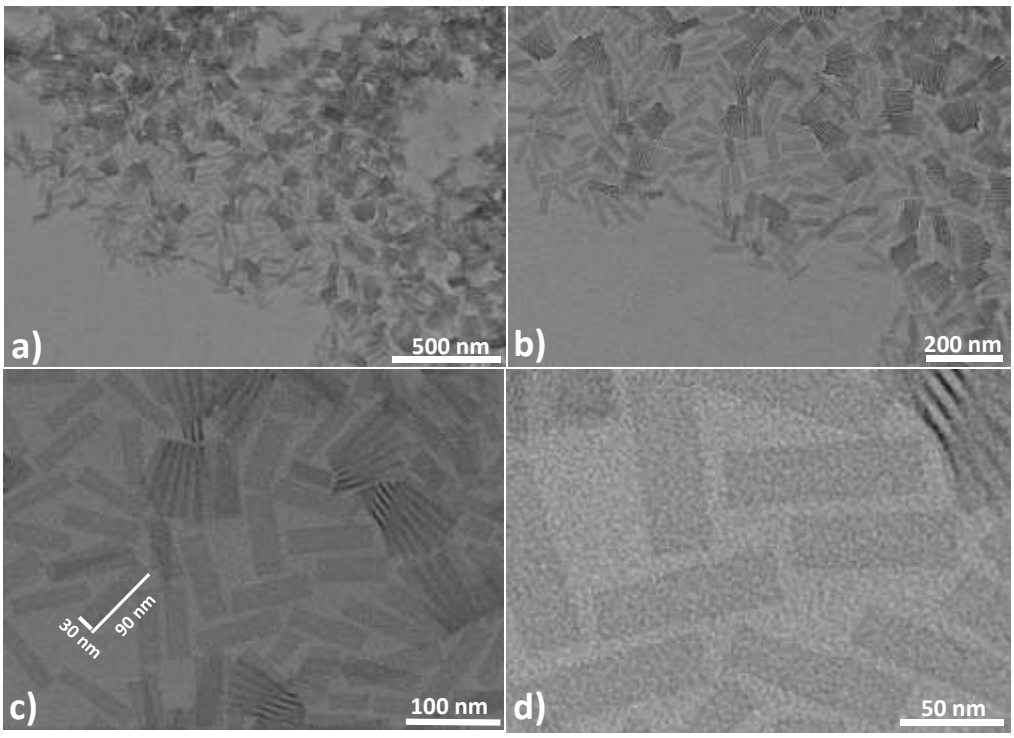

Figure 3.2: (a-d) TEM images of CdSe/CdSeTe NPL.

3.1.3 Surface structural analysis via XPS

3.1.3.1 XPS Analysis of CdSe/CdSeTe core/crown NPL

In order to inspect the surface chemistry and elemental composition of the core/crown NPL, XPS analysis was performed. Figure 3.3 displays XPS analysis results for CdSe/CdSeTe NPL in the absence of P25 where binding energy (B.E) positions of the spectrums were calibrated using the surface carbon signal at 284.8 eV. As mentioned in previous sections, CdSe/CdSeTe NPL are capped with oleic acid, therefore additional oxygen and carbon signals are also detected in XPS spectra. In the O1s spectrum (Figure 3.3.a), a broad and a convoluted signal is observed which can be associated with the C-O, C=O and O-H functionalities of the oleic acid capping of the NPL [71]. Figure 3.3.b presents the corresponding C*1s* spectrum of the fresh NPL, where the shoulder visible at 288.1 eV can be ascribed to C-O and C=O

functionalities of the oleic acid capping and the larger signal at 284.8 eV can be attributed to C-C linkages of oleic acid as well as the surface (adventitious) carbon species.. Considering the XPS data for the Cd, Se and Te regions, it can be clearly seen that the corresponding B.E. values show close resemblance to the quantum dot systems containing heterojunctions including both CdSe and CdTe domains [72]–[74]. Thus, observed Cd$3d_{5/2}$ feature at 405.1 eV in Figure 3.3.c is consistent with the Cd species interacting with Te and/or Se species and lack of significant amounts of CdO_x species [72]–[74]. The Te$3d_{5/2}$ feature located at 572.5 eV in Figure 3.3.d corresponds to Te species that are in interaction with Se and/or Cd [72]–[76]. Similarly, the broad and complex Se*3d* signal in Figure 3.3.e shows a Se$3d_{5/2}$ B.E. of *ca.* 53.9 eV in agreement with the existence of CdSe and CdSeTe species. XPS results given in Figure 3.3 are consistent with the presence of closely interacting Cd, Se and Te species as would be expected in the CdSe/CdSeTe NPL.

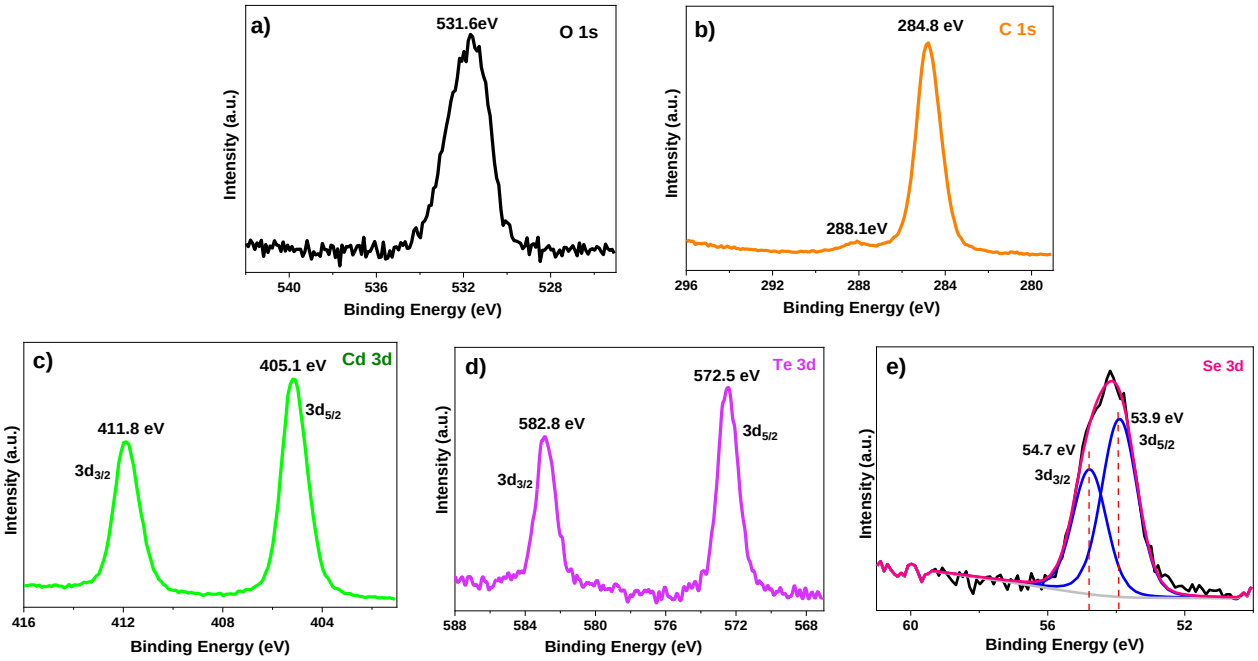

Figure 3.3: XPS spectra of CdSe/CdSeTe NPL (in the absence of TiO_2): a) O*1s*, b) C*1s*, c) Cd*3d*, d) Te*3d*, and e) Se*3d* regions.

3.1.3.2 XPS Analysis of CdSe/CdSeTe/P25 composites

XPS results for CdSe/CdSeTe/TiO_2 composite system in its fresh (as prepared) form, as well as after 5 h aging under PHONOS reaction conditions with UV-A or VIS illumination are presented in Figures 3.4 and 3.5, respectively. It is important to note that, B.E. positions of the spectra in Figures 3.4 and 3.5, were corrected using the Ti*2p* signal of the TiO_2 component due to the presence of a large amount of carbonaceous species which were initially existing on the TiO_2 (P25) support, rendering the use of the surface carbon species difficult for the B.E. calibration. In Figure 3.4.a, Ti$2p_{3/2}$ and Ti$2p_{1/2}$ features of P25 (TiO_2) can be observed at 458.5 eV and 464.1 eV respectively, consistent with the typical Ti^{4+} species in the titania structure. It is observed in Figure 3.4.a. that functionalization of TiO_2 with the oleic acid capped CdSe/CdSeTe NPL leads to an expected decrease in the Ti*2p* signal of the TiO_2 component due to shielding of the underlying titania with the adsorbed surface functionalities. However, after 5 h PHONOS reaction under UV-A irradiation, Ti*2p* signals of TiO_2 increases slightly compared to the fresh sample. It seems that, UV-A aging results in a partial recovery of the Ti*2p* signal, suggesting an increasing exposure of the titanium surface species to the incoming X-rays , that happens as a result of photochemical changes and degradation in the oleic acid-capped CdSe/CdSeTe NPL overlayer. This observation is also in line with the observed changes in the XPS data in Figures 3.4.b and 3.4.c, in which the oleic acid capped CdSe/CdSeTe NPL functionalization of P25 increases the C*1s* and O*1s* signals as compared to that of pure P25. However, UV-A aging results in the attenuation of the corresponding C*1s* and O*1s* signals. Additional broadening in the C-O and C=O functionalities of the oleic acid capping agent is observed (Figure 3.4.b) at 288.1 eV, suggesting relatively small but noticeable photochemically-induced changes/degradation in the functional groups of the oleic acid capping agent. The P25 XPS spectrum given in Figure 3.4.d reveals two loss features of Ti2s

located ca. 590 and 578 eV [77], where the lower B.E. Ti*2s* loss feature overwhelms the Te*3d* region. Due to the presence of this particular Ti*2s* loss feature, a clear information regarding the oxidation state changes of Te upon UV-A aging cannot be achieved. Se XPS signals in the CdSe/CdSeTe/TiO_2 composite system were not detectable due to: *i)* small X-ray photoionization cross-section of Se XPS peaks, *ii)* small NPL loading, iii) overlap of Se XPS peaks with other XPS features.

XPS spectra of Cd*3d* region of CdSe/CdSeTe/TiO_2 composite is shown in Figure 3.4.e. Binding energy shift observed in Cd*3d* peak for UV-A aged CdSe/CdSeTe/TiO_2 sample suggests that electronic structure changes occurs in Cd upon UV-A aging due to photo-oxidation of Cd species with atmospheric oxygen, water, and/or CO_2, as well as due to the changes in the chemical environment of Cd and Te surface species upon partial photo-degradation of the overlying oleic acid capping agent.

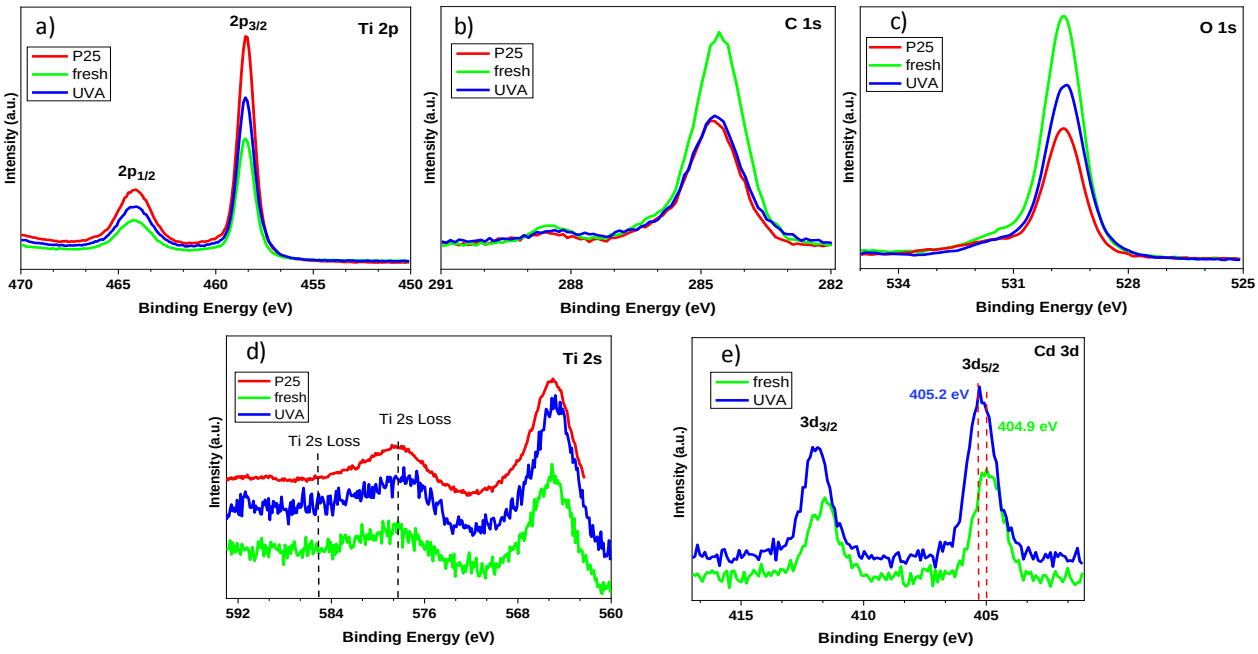

Figure 3.4: XPS spectra of fresh (green curves) and UV-A-aged (blue curves) CdSe/CdSeTe/TiO_2 composite system and pure TiO_2 (red curves) under PHONOS reaction: a) Ti*2p*, b) C*1s*, c) O*1s* d) Te*3d*/*Ti2s*, and e) Cd*3d* regions.

Figure 3.5. demonstrates the XPS analysis of the CdSe/CdSeTe/TiO_2 composite system after VIS-aging under PHONOS reaction. Ti*2p* spectra is presented in Figure 3.5.a. Ti$2p_{3/2}$ and Ti$2p_{1/2}$ features of P25 are observed at 458.5 and 464.1 eV and correspond to Ti^{4+} species in agreement with the literature [75]. It is also clear in Figure 3.5.a that, oleic acid used capping agent in CdSe/CdSeTe NPL leads to a decrease in TiO_2 Ti*2p* signal intensity due to the blocking of the underlying titania with the adsorbed surface functionalities. Figure 3.5.a also reveals that Ti*2p* intensities slightly rise after VIS aging under PHONOS condition. Therefore, it can be argued that, VIS aging leads to a partial recovery of the Ti*2p* signal, suggesting an improved exposure of the surface titanium species to the incoming X-rays due to photochemical degradation and changes of the oleic acid-capping during VIS-aging. The XPS spectra of C*1s* and O*1s* regions are shown in Figures 3.5.b and 3.5.c which are in accordance with the behavior of the XPS spectra given in Figure 3.5.a, where C*1s* and O*1s* signal intensities of the oleic acid-capped CdSe/CdSeTe NPL functionalization of P25 increases as compared to that of pure titania . As in the case of the UV-A aging results presented in Figures 3.4.b and 3.4.c, VIS aging results provided in Figures 3.5.b and 3.5.c also demonstrates a decline in the signal intensities corresponding to C*1s* and O*1s*. Furthermore, according to Figure3.5.b, VIS aging gives rise to shifting/broadening of the C*1s* peaks *ca.* 288.1 eV, indicating relatively small but measurable photochemically-induced changes/degradation of the capping agent. Ti*2s* XPS spectrum of P25 and Te*3d* XPS spectra of fresh and VIS aged CdSe/CdSeTe/TiO_2 composite system are given in Figure 3.5.d. Clear information regarding the oxidation state change of Te upon VIS-aging is not achievable due to Ti*2s* loss feature of P25 overwhelming Te$3d_{5/2}$ region. Similar to Figure 3.4.d. Figure 3.5.e reveals the XPS spectra of Cd*3d* before and after the VIS-aging. Similar to Cd*3d* spectra given in Figure 3.3.c, B.E. of Cd$3d_{3/2}$ *and* Cd$3d_{5/2}$ are in harmony with the Cd species interacting with Te and/or Se species [72]–[74]. A blue shift in Cd*3d* B.E is also observed which is consistent with the blue shift observed for Cd*3d* presented

in Figure 3.4.e. However, the B.E. shift observed in Figure 3.5.e is smaller than that of the B.E. shift observed in Figure 3.4.e in terms of magnitude. This smaller shift to higher B.E. in Cd*3d* for VIS experiments suggests that electronic structure of the NPL is subjected to smaller changes upon VIS aging as compared to that of UV-A aging. In other words, CdSe/CdSeTe/TiO_2 composite system is more stable under VIS irradiation as compared to UV-A irradiation.

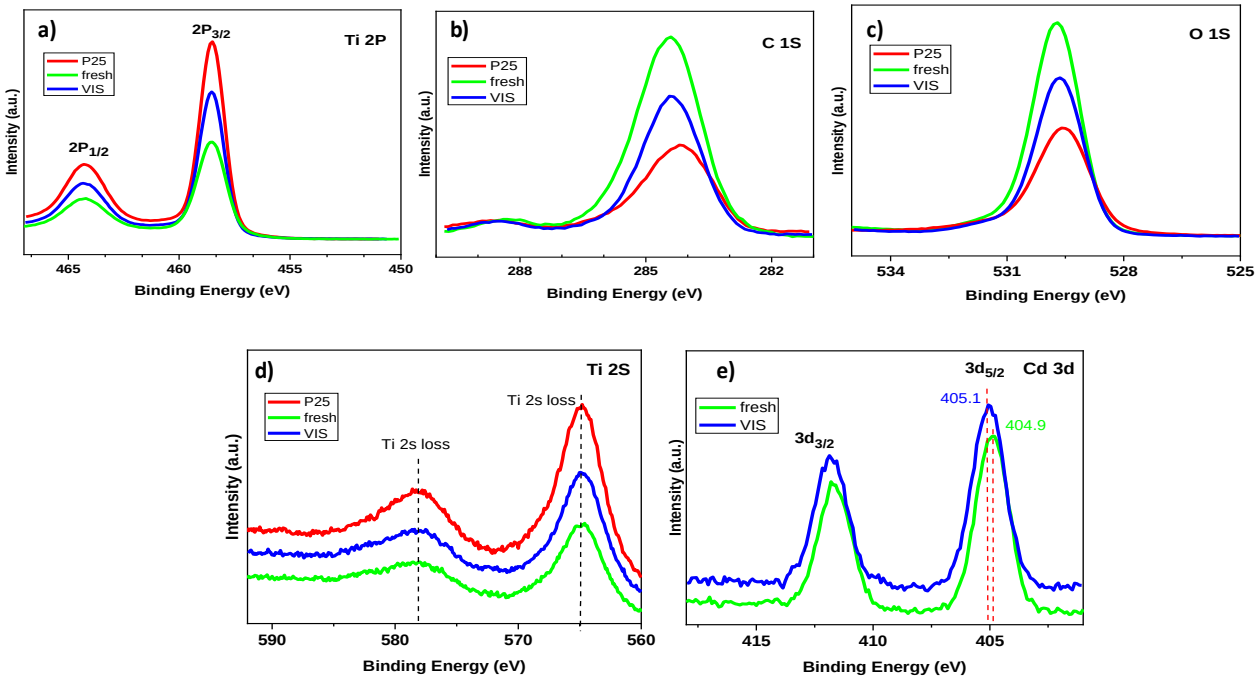

Figure 3.5: XPS spectra of fresh (green curves) and VIS-aged (blue curves) CdSe/CdSeTe/TiO_2 composite system and pure TiO_2 (red curves) under PHONOS reaction: a) Ti*2p*, b) C*1s*, c) O*1s* d) Te*3d/Ti2s*, and e) Cd*3d* regions.

3.1.4 Specific surface area (SSA) analysis with BET

Specific surface areas were determined by the conventional Brunauer-Emmett-Teller (BET) procedure. SSA of pure P25 was found to be 50 m^2/g, while addition of NPL to P25 resulted in slight changes where, the SSA of 0.05NPL/P25, 0.1NPL/P25, 0.5NPL/P25,

1.0NPL/P25 and 2.0NPL/P25 were determined to be 44, 45, 41, 40 and 39 m^2/g, respectively. This trivial decline in SSA with increasing NPLs loading can be ascribed to the partial blocking of the P25 pores by oleic acid capped NPL with dimensions of 90 nm × 30 nm.

3.1.5 Electronic structural analysis via DR-UV-A-VIS and Photoluminescence spectroscopy

Absorption spectrum of core/crown CdSe/CdSeTe NPL (in the absence of TiO_2) is presented in Figure 3.6. It reveals light-hole (lh) transitions of the CdSe core of CdSe/CdSeTe NPL at 482 nm. Heavy-hole (hh) peak position of CdSe core is also demonstrated in Figure 3.6 which is centered at 512 nm [77]. These sharp excitonic transitions in the absorption spectrum of CdSe core remain almost unchanged during the lateral growth of CdSeTe crown, irrespective of CdSeTe crown size. Lateral growth of CdSeTe-crown layers on CdSe core seed, leads to a new absorption peak at 563 nm for CdSe/CdSeTe NPL due to the light-hole electron transition in the CdSeTe crown, [78]. Absorption spectrum of CdSe/CdSeTe core/crown NPL confirms the formation of type-II band alignment of NPL heterojunctions as both CdSe core and CdSeTe crown contribute to absorption spectrum.

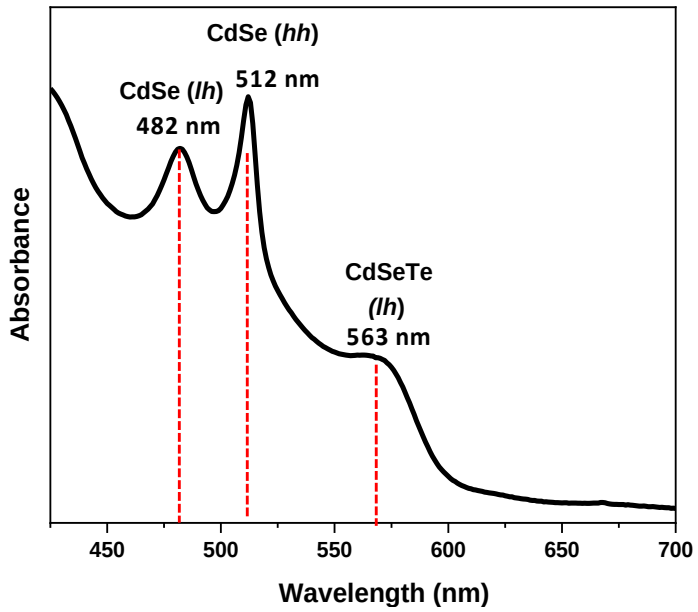

Figure 3.6: Absorption spectrum of 4ML-thick core/crown CdSe/CdSeTe quantum well nanoplatelets Ref [77].

Tauc Equation is used to calculate the bandgap energy of the synthesized CdSe/CdSeTe NPL given in Equation 41 [32].

$$(\alpha h\nu)^n = A\,(h\nu - E_g) \qquad (41)$$

Where, E_g is the band gap, h stands for Planck's constant, ν represents frequency of the photon, α is the absorption coefficient and A is the proportionality constant. The value of the exponent "n" denotes the nature of the electronic transition, (*i.e.* direct or indirect). For a direct bandgap material, n equals to 2, whereas for an indirect bandgap material n is equal to 1/2. The bandgap values can be estimated from the intercept of the linear portion of the $(\alpha h\nu)^n$ vs. hν plots on the hν axis. Figure 3.7 illustrates the Tauc plot for the CdSe/CdSeTe NPL (without P25) revealing a direct band gap of 2.4 eV for the CdSe core and 2.1 eV for the CdSeTe crown.

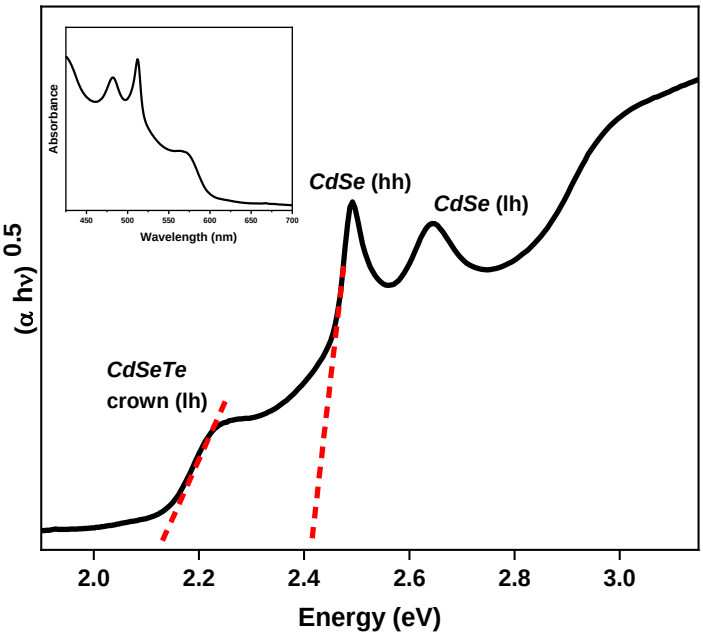

Figure 3.7: Tauc plot and bandgap calculation for CdSe/CdSeTe NPL.

Photoluminescence (PL) spectrum of core/crown NPL is given in Figure 3.8 showing an emission peak centered at 591 nm with a full width at half maximum (FWHM) of 45 nm.

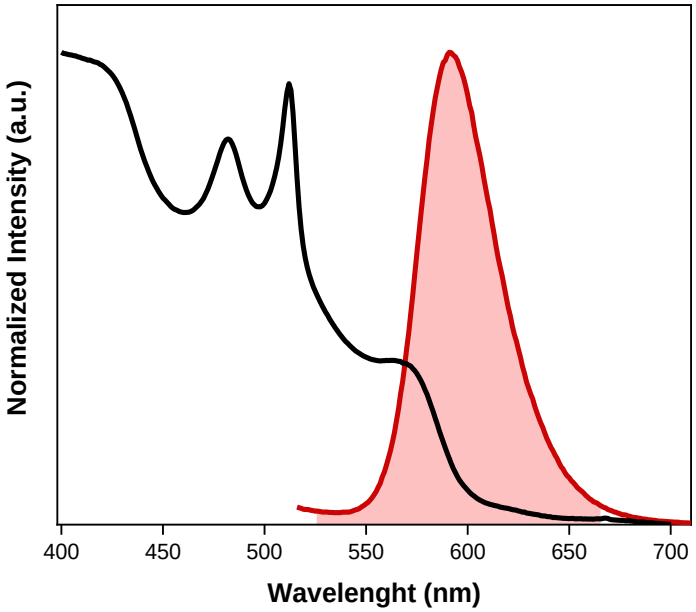

Figure 3.8: PL spectra of core/crown Cedes/CdSeTe quantum well NPL[77].

Diffuse reflectance UV-VIS Spectroscopy (DRS) is used to elucidate the electronic band structure of the synthesized materials. A Kubelka- Munk function given in Equation 42, can be applied to DRS spectrum, where R is the absolute reflectance, k is the molar absorption coefficient and s is the scattering coefficient.

$$F(R) = \frac{(1-R)^2}{2R} = \frac{k}{s} \qquad (42)$$

Since F(R) is proportional to the absorption coefficient (α), using Equation 41, transformed Kubelka-Munk function (Tauc plot) can be obtained as shown in Equation 43, which relates the incident photon energy (hν) and the optical bandgap energy [79].

$$[\,F(R)h\nu]^n = A\,(h\nu - E_g) \qquad (43)$$

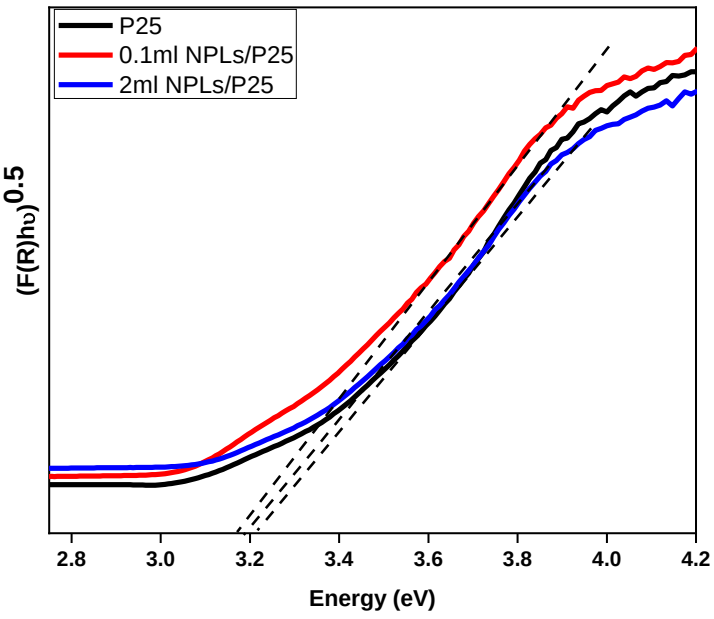

Figure 3.9: Tauc plot and bandgap calculation for P25, 0.1NPL/P25 and 2NPL/P25.

Therefore, by plotting $[F(R)h\nu]^2$ against hν, bandgap values can be obtained. As can be observed in Figure 3.9, the obtained bandgap values for P25 and two different loadings of NPLs on P25 are roughly 3.2 eV, and incorporation of CdSe/CdSeTe NPLs does not lead to a significant change in the bandgap of P25.

Using Equations 44 and 45 [80] and bandgap energies of various structural components in the NPL and NPL/TiO_2 system (*e.g.* CdSe, CdSeTe, and TiO_2) determined from Figures 3.7 and 3.9, the valance band and conduction band positions of these compounds were estimated.

$$E_c^0 = E_e - X_{AB} + 0.5\, E_g \quad (44)$$

$$X_{A_xB_y} = \sqrt[x+y]{X_A^x . X_B^y} \quad (45)$$

In Equations 44 and 45, E_c is the conduction band potential, X_{AB} is the electronegativity of the semiconductor expressed as the geometric mean of the absolute electronegativity of the constituent atoms, x and y are stoichiometric coefficients in the empirical formula, E_e is the energy of free electrons on the hydrogen scale (*i.e.* 4.5 eV) and E_g is the bandgap [81]. Schematic representation of band structure for the CdSe/CdSeTe/TiO_2 system, based on the estimated energy positions are summarized in Figure 3.10. Since the conduction band edge of CdSe core lies lower in energy than that of CdSeTe crown, excited photoelectrons in the conduction band of the CdSeTe crown can be transported to the conduction band of the CdSe core which can eventually be transferred to the conduction band of the TiO_2 during the photoexcitation of CdSe/CdSeTe/P25 system. Accordingly, generated holes can be confined in the CdSeTe crown valance band. This electron transfer cascade may yield an efficient electron-hole separation, extended exciton lifetime and suppression of the electron-hole recombination

processes, which is responsible for the photocatalytic activity enhancement of the CdSe/CdSeTe/TiO_2 composite system studied in the current work.

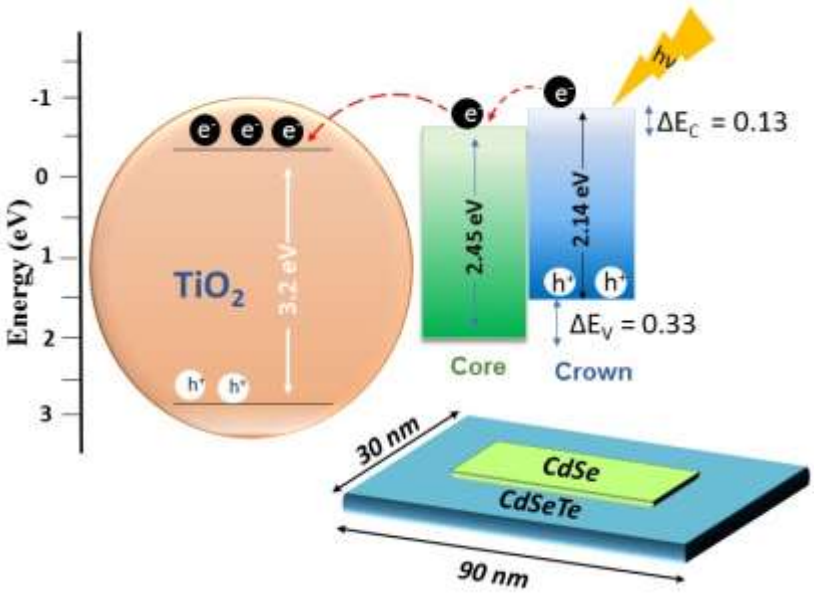

Figure 3.10: Electron energy diagram for core/crown CdSe/CdSeTe NPL on TiO_2.

3.1.6 Electron and hole trapping analysis of CdSe/CdSeTe NPL via EPR Spectroscopy

In an attempt to elucidate the influence of UV irradiation on the electronic structure of the CdSe/CdSeTe NPL, *in-situ* EPR experiments were conducted under both dark and 2 h-long UV irradiation. The main objective here is to detect the delocalized electrons or holes trapped on the surface of NLPs which can be formed by exposing CdSe/CdSeTe NPL to UV irradiation. In the former studies, electrons trapped in the colloidal InP system upon optical excitation were investigated by *in-situ* EPR studies [82]. Because the typical life times of such electron trapping events are relatively short (in the order of 10^{-9}-10^{-3}), long-life time (10^{1}-10^{2} s) radical spin traps such as 2,2,6,6-tetramethylpiperidin-1-yl) oxidanyl (TEMPO) or 5,5-dimethyl-pyrroline N-

oxide (DMPO) or metal cation dopants such as Mn^{2+} were added to the analyzed samples to allow longer data acquisition times with a higher signal to noise ratio (S/N).

In the current *in-situ* X-band EPR measurements, no external spin-trap agents were added to the measured samples. In Figure 3.11, no detectable EPR signals for CdSe/CdSeTe NPL in dark is observed. However, UV irradiation leads to the appearance of a new EPR signal implying the generation of paramagnetic states in NLPs. Taking into account the corresponding g-factor of the detected EPR signal, the new signal which is occurring only in the presence of UV irradiation can be attributed to photo-induced electron transfer from the CdSeTe crown to the CdSe core of the quantum well NPL system, where electron-trapping occurs in the CdSe core. While trapped electrons and trapped holes yield similar g-values (g_e = 2.0023 [79]) in EPR, detection of trapped hole states in EPR is difficult due to the significantly smaller EPR intensities of the hole states. Thus, current EPR data supports the synergistic electronic effect of the CdSe/CdSeTe NPL in the CdSe/CdSeTe/TiO_2 composite system extending the electron-hole recombination lifetime which presumably has a positive effect on the photocatalytic activity, as will be explained in the further sections. Note that EPR signals for the experiments performed on CdSe/CdSeTe/TiO_2 were below the detection limit, due to the small concentration of NPL present in the NPL/P25 system and so they are not shown here. It is important to note that, no EPR signals is observed for P25 TiO_2 neither under dark nor UV irradiation.

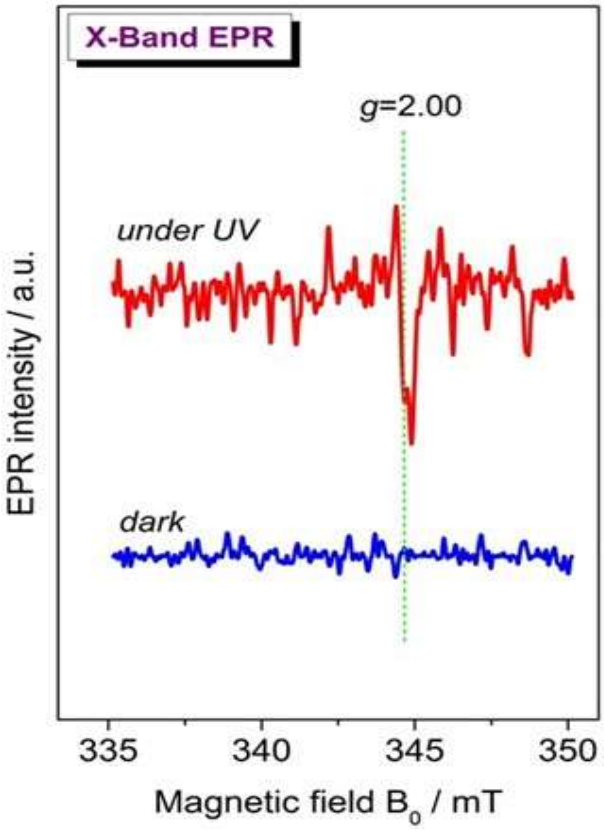

Figure 3.11: Room temperature X-band EPR spectra of CdSe/CdSeTe NLPs (without TiO_2) under dark and UV illumination conditions.

3.2 Photocatalytic NO_x(g) Oxidation and Storage (PHONOS) Performance Tests

Photocatalytic NO_x oxidation and storage performances of CdSe/CdSeTe/P25 composites were measured and compared to benchmark Degussa P25 TiO_2. The analysis and interpretation of the photocatalytic performance of catalysts were made based on %NO Conversion, %NO_x Storage selectivity, DeNO_x index and % Photonic efficiency values.

3.2.1 Photocatalytic performance of P25 under UV-A and VIS irradiation

In the first step, photocatalytic activity tests were performed for fresh and aged P25 TiO_2 under UV-A as well as VIS irradiation. As mentioned before, aged samples were prepared by

exposing the catalyst to UV-A or VIS light source for 18 h under ambient conditions prior to the photocatalytic activity measurements. It can be observed from Figure 3.12 that, P25 has a relatively high and acceptable NO conversion of 33%. On the other hand, it shows an extremely low NO_x storage selectivity (23%) as a result of the production of large quantities of unwanted NO_2(g) under UV-A irradiation. Electronic structures of NO and NO_2 reveal a radical nature with an unpaired valance electron. On the other hand, NO_2(g) is more likely to be adsorbed on TiO_2 surface, partly due to its higher electron affinity (2.27 eV) compared to NO(g) (0.026 eV) [83]. However, photocatalytic NO_2(g) production rate and the total amount of generated NO_2 throughout the photocatalytic reaction, readily overcomes the NO_x adsorption capacity of TiO_2 leading to unwanted NO_2(g) release into the atmosphere which results in extremely negative DeNO_x index values (-0.42 and -0.45 for fresh and aged P25, respectively) shown in Figure 3.13. After irradiation under UV-A light for 18 h, a slight decrease in activity is observed for aged sample. Obtained results suggest that P25 TiO_2 is active in NO photo-oxidation, however its selectivity towards NO_x capture/storage is extremely limited. Therefore, it does not qualify as an efficient photocatalyst for NO_x abatement under UV-A light irradiation.

Photocatalytic activity of P25 TiO_2 under VIS irradiation is also revealed in Figures 3.12-3.14. Fairly good NO conversion and NO_x storage selectivity under VIS irradiation is obtained (as in the case of UV-A irradiation). It is worth to note that even though P25 TiO_2 is widely considered to be a UV-active photocatalyst, current findings indicate promising PHONOS activity under VIS illumination as well. This can be due to the presence of anatase (78-85%), rutile (14-17%) and amorphous domains present in P25 providing a variety of heterojunctions which may also reveal significant photocatalytic NO conversion under VIS-light.

Additionally, the photon flux values currently used for VIS experiments were greater than those of the UV-A experiments. Consequently, % photonic efficiency results presented in

Figure 3.14, exhibit lower NO_x storage % photonic efficiency for P25 under VIS illumination compared to that of UV-A due to the normalization of conversion values with photon flux in the photonic efficiency % definition. Both illumination sources reveal rather similar % NO conversion and % NO_x storage Selectivity (Figure 3.12). Hence it can be deduced that, % NO conversion values achieved for VIS light experiments are due to a greater photon flux and a lower quantum efficiency. Moreover, fresh and aged P25 samples lead to significantly negative and unfavorable DeNO_x index values under VIS-light illumination, suggesting that P25 cannot effectively store photogenerated NO_2 and instead, releases toxic NO_2(g) into the atmosphere.

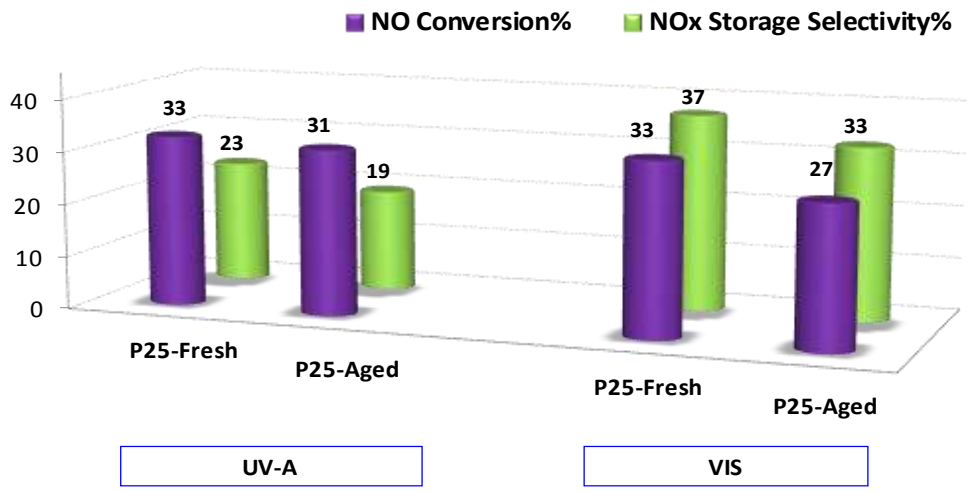

Figure 3.12: NO(g) conversion %, and NO_x storage selectivity % for fresh and aged P25 under UV-A & VIS illumination.

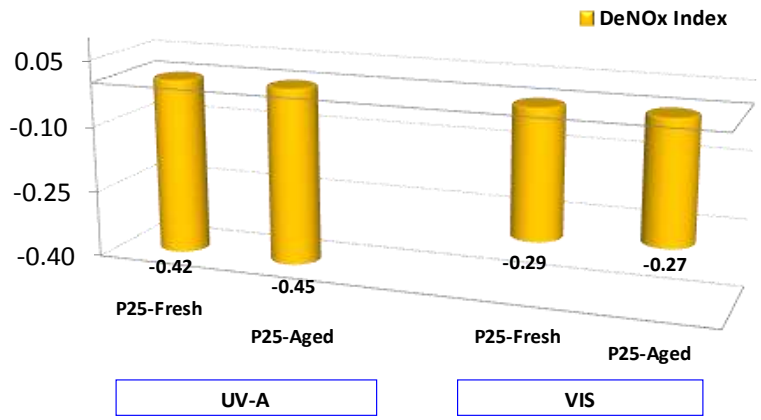

Figure 3.13: DeNO_x index values for fresh and aged P25 under UV-A & VIS illumination.

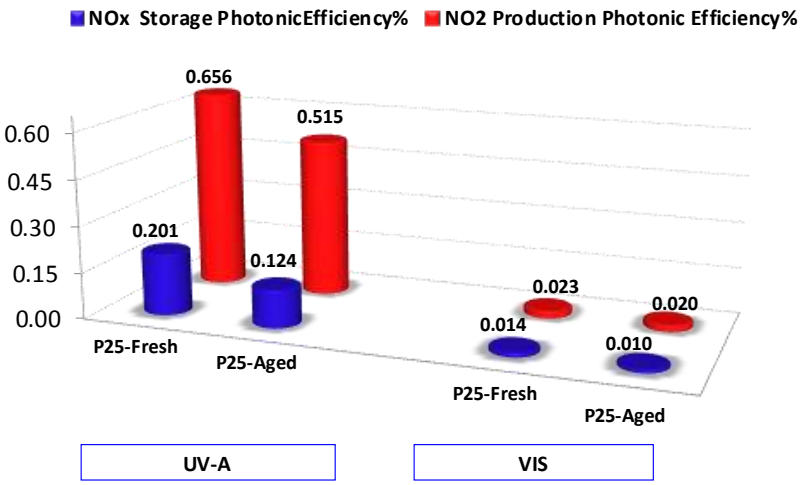

Figure 3.14: % Photonic efficiency of P25 under UV-A & VIS illumination.

3.2.2 Photocatalytic performance of fresh and aged CdSe/CdSeTe/P25 catalysts under UV-A light

Photocatalytic activity tests were conducted for fresh and aged CdSe/CdSeTe/P25 photocatalysts with different NPL loadings and were compared with commercial benchmark P25 TiO_2 photocatalyst under identical experimental conditions. It can be observed in Figure 3.15 that, incorporation of different loadings of CdSe/CdSeTe NPL to P25 leads to overall

improvement in PHONOS performance under UV-A irradiation. Even for very small loading of NPL (0.05 ml) %NO conversion and % NO_x storage selectivity increase significantly and reach 41% and 81%, respectively for fresh 0.05 NPL/P25 under UV-A illumination

By increasing NPL loading to 0.1-2 ml, PHONOS performance of fresh NPL/P25 increases monotonically and a maximum of 44% for % NO conversion and 94% for selectivity are achieved for 2.0 NPL/P25 photocatalyst. Slight increase in % NO conversion upon NPL addition is attributed to the presence of CdSe/CdSeTe NPL which provide additional adsorption sites for NO_x storage products and prevent the saturation of TiO_2 's active sites which are primarily responsible for photocatalytic oxidation. On the other hand, further increase in NPL loading (*i.e.* for 6.0NPL/P25) result in a drastic decline in % NO conversion. Since the photocatalytic active sites reside on TiO_2, the attenuation in performance in high loadings may be due to the blockage of active sites or substitution of the surface -OH functionalities of TiO_2 with oleic acid capped-NPL. It is evident that fresh 2.0NPL / P25 photocatalyst is capable of storing considerable amounts of NO_x in solid state, while substantially suppressing NO_2(g) release under UV-A irradiation. These results (Figures 3.15 - 3.17) clearly show that, proper loadings of NPL used in the functionalization of P25 TiO_2 modifies the unfavorably negative DeNO_x index of pure P25 TiO_2 (−0.42) to a significantly positive value (+0.35) under UV-A illumination. % Photonic efficiency results given in Figure 3.17 is also in line with given data in Figures 3.15 and 3.16. Where NO_2 release efficiency declines significantly, and NO_x storage efficiency raises drastically by addition of CdSe/CdSeTe NPL and a volcano-type plot is observed where an optimum performance was obtained for 2.0 NPL/P25.

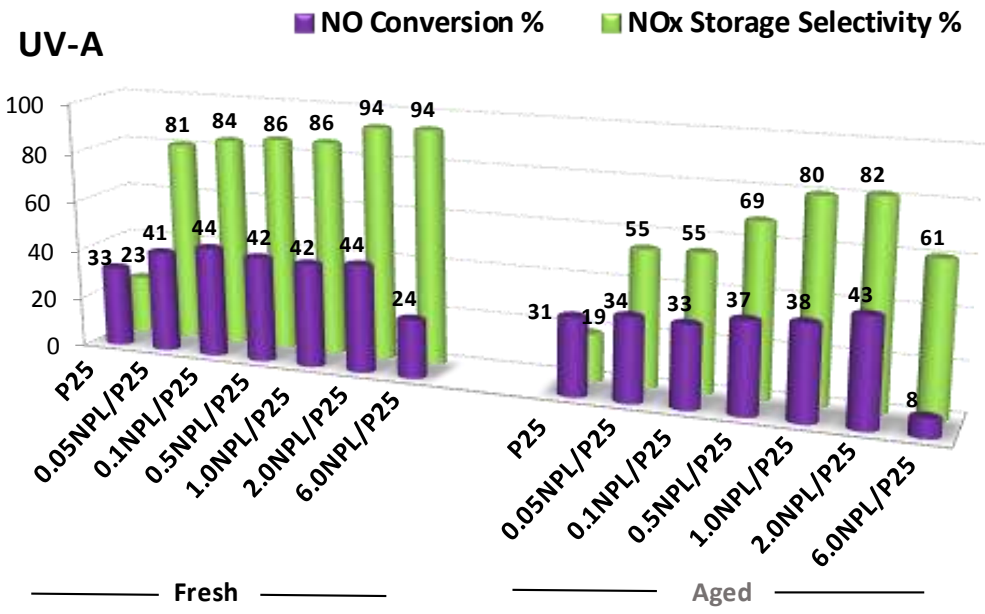

Figure 3.15: % NO(g) conversion and %NO_x storage selectivity values for P25 and NPL/P25 under UV-A light for fresh and aged samples.

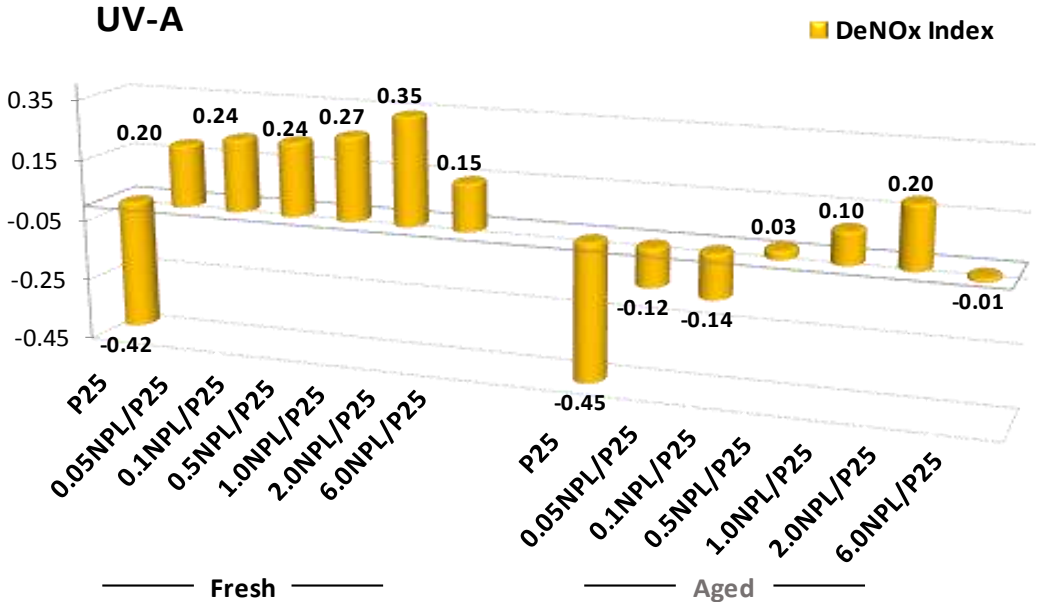

Figure 3.16: DeNO_x Index values for P25 and NPL/P25 under UV-A light for fresh and aged samples.

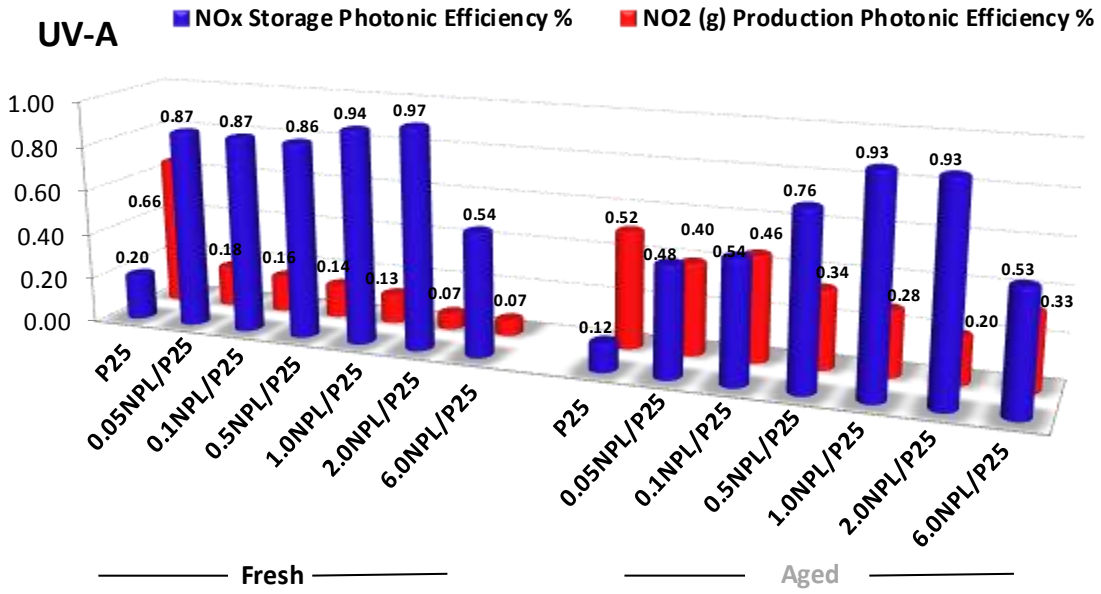

Figure 3.17: % Photonic efficiency values for P25 and NPL/P25 under UV-A light for fresh and aged samples.

UV-A aging of the NPL/P25 photocatalysts in 18 h under ambient conditions leads to interesting changes in the photocatalytic performance trends. Even although, NO conversion is not significantly influenced by UV-A aging for the NPL loadings within 0.05 - 2.0 mL, NO_x storage selectivity severely decreases (Figure 3.15) Nevertheless, regardless of the loss in PHONOS performance, some of these aged photocatalysts are able to yield significantly positive DeNO_x index values and exceed P25 TiO_2 benchmark. The Degradation/decomposition of the oleic acid capping of the CdSe/CdSeTe NPL may be responsible for the decrease in photocatalytic performance of the NPL/P25 system upon UV-A aging [84]. One other possibility is the electronic changes in the CdSe and CdSeTe domains such as oxidation of Cd sites and reduction of Te sites, as suggested in XPS results given in Figure 3.4. It is worth mentioning that NO conversion capability of the NPL/P25 system is only slightly affected after UV-A aging (Figure 3.15), signifying that majority of the active sites for the photocatalytic NO oxidation on TiO_2 surface remained unchanged and could still function

effectively even after 18 h aging under UV-A. This is in line with the absence of any oxidation state changes in the Ti*2p* XPS signal of P25 TiO_2 domains before and after aging given in Figure 3.4. On the other hand, aging of 6.0 NPL/P25 system with the highest NPL loading results in an extreme loss in both NO conversion activity as well as in NO_x storage selectivity. This is possibly because of the widespread blocking of the photocatalytic active sites and NO_x storage sites of TiO_2 and CdSe/CdSeTe domains of the 6.0NPL/P25 system due to high loading with the abundant oleic acid degradation products; apparent by the very low DeNO_x index of aged 6.0NPL/P25 (-0.01), as revealed in Figure 3.16.

3.2.3 Photocatalytic performance of fresh and aged CdSe/CdSeTe/P25 catalysts under VIS light

The effect of VIS light irradiation on photocatalytic activity of different loadings of NPL on P25 were examined and PHONOS performances of CdSe/CdSeTe/P25 are shown in Figures 3.18-3.20. As can be seen, there is a minor increase in % NO conversion along with a drastic improvement in % NO_x storage selectivity by incorporation of NPL onto P25 % under VIS irradiation. Fresh 0.1 NPL/P25, demonstrated 38% NO conversion, 93% selectivity along with the most positive DeNO_x index value of +0.30, and provided the highest PHONOS performance. The best performance under VIS irradiation was obtained at relatively lower loadings of NPL on P25 (0.1 NPL/P25) compared to the UV-A case (2.0 NPL/P25). Comparison of the photocatalytic activity results of NPL/P25 with benchmark P25 suggests while there is only a slight enhancement in the % NO conversion upon NPL functionalization, an impressive improvement in selectivity (*i.e.* an increase from 37% for P25 to 95% for NPL/P25) was observed for NPL/P25, leading to a very positive DeNO_x index value for the latter catalyst as shown in Figure 3.19. As mentioned in the previous section, current findings

suggest that, the photocatalytic NO conversion was mostly carried out by TiO_2 sites and the primary photocatalytic sites for NO oxidation on the NPL/P25 system resides on P25 TiO_2, while a synergistic effect between TiO_2 and NPL results in a further increase in NO conversion capability. On the other hand, the most forthcoming function of oleic acid-capped NPL is the photocatalytic conversion and storage of photogenerated NO_2 species into other oxidized surface species, such as HONO, $HONO_2$, NO_2^- and NO_3^-. It is obvious that extremely high loadings of NPL on P25, has a detrimental influence on PHONOS performance of NPL/P25 catalysts due to the blocking of the TiO_2 active sites with NPL.

Effect of 18 h VIS aging on PHONOS performance is also examined. Figure 3.18 demonstrates that % NO conversion of NPL/P25 decreases after VIS aging compared to fresh catalysts and leads to lower rates of NO_2(g) generation, providing an efficient NO_x capture by the photocatalyst which results in a higher NO_x storage selectivity %, and consequently positive DeNO_x index values (Figure 3.19). These changes in performance are also demonstrated in Figure 3.20 in terms of %photonic efficiency.

It is important to note that the VIS-aging effect on the overall performance of NPL/ P25 (Figures 3.18-3.20) is relatively less drastic as compared to that of UV-A-aging (Figures 3.15-3.17), possibly due to the higher stability of NPL and oleic acid capping agent under VIS irradiation as corroborated by the current XPS data given in Figures 3.4 and 3.5.

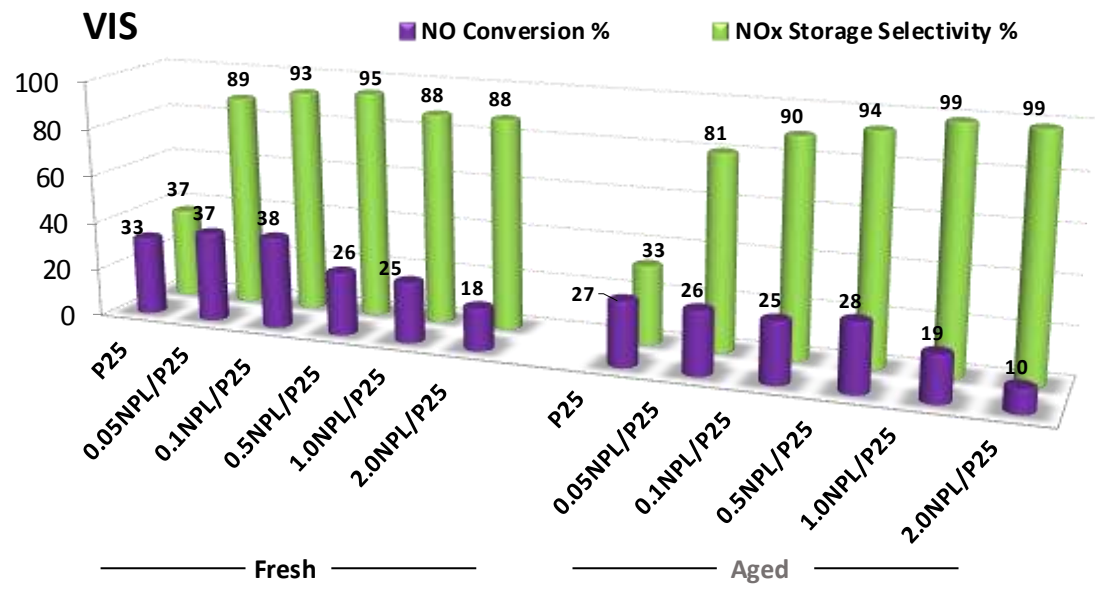

Figure 3.18: % NO(g) conversion and %NO_x storage selectivity values for P25 and NPL/P25 under VIS light for fresh and aged samples.

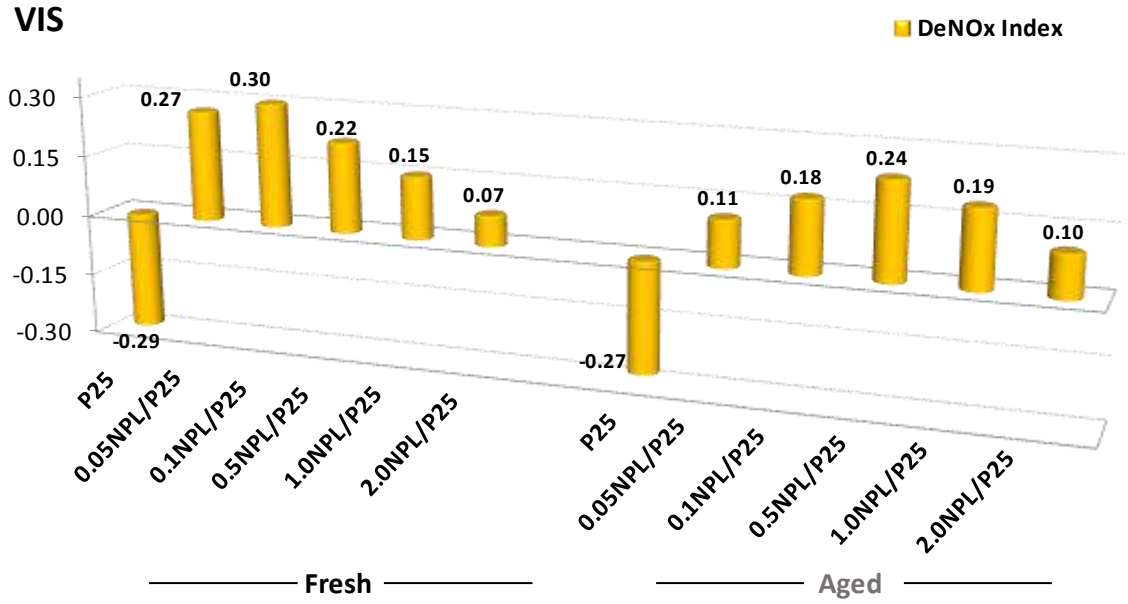

Figure 3.19: DeNO_x index values for P25 and NPL/P25 under VIS light for fresh and aged samples.

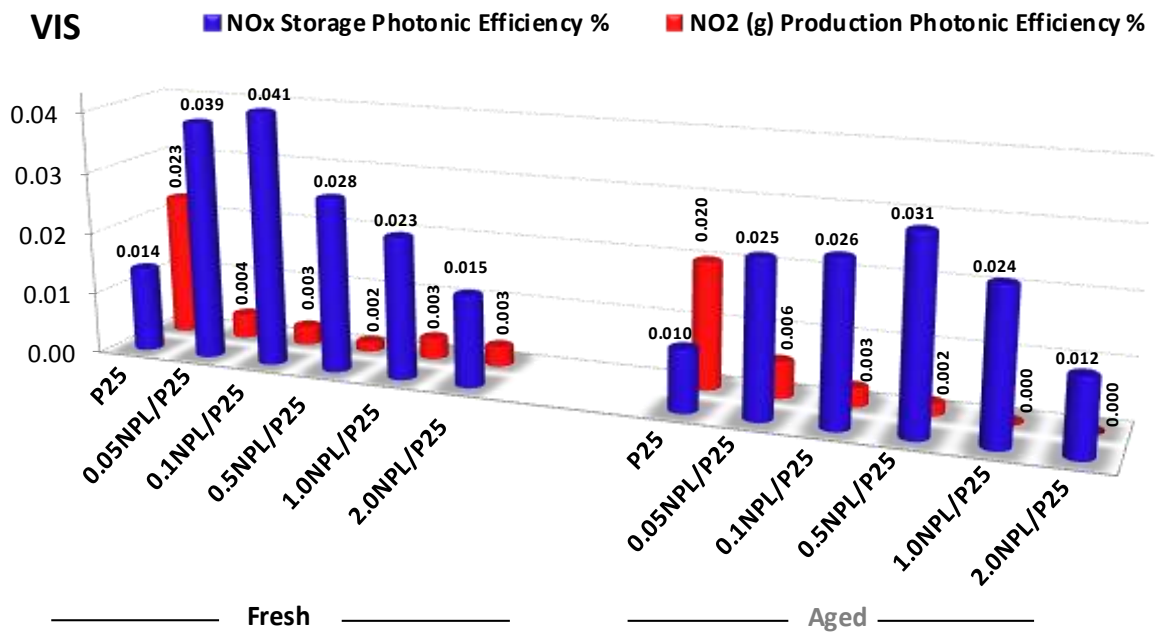

Figure 3.20: % Photonic efficiency values for P25 and NPL/P25 under VIS light for fresh and aged samples.

3.2.4 Effect of NPL dispersion medium (toluene) on the photocatalytic performance of P25

In the current study, CdSe/CdSeTe NPL were dispersed in toluene ($C_6H_5CH_3$ (*l*)). Therefore, it is important to understand whether toluene adsorption on P25 affects the PHONOS performance. Additional control experiments were carried out for this purpose by adding varying amounts of $C_6H_5CH_3$ (*l*) on P25 at RT accompanied by drying at 70 ˚C for 18 h similar to the procedure used in NPL/P25 sample preparation. Along these lines, fresh and UV-A or VIS-aged T/P25 samples were prepared using the same volumes selected for the preparation of the NPL/P25 composite systems and PHONOS activity tests were performed under UV-A and VIS light irradiation. It is interesting to mention that addition of Toluene to P25, leads to an increase in %NO conversion and % NO_x Storage selectivity of fresh samples both under UV-A and VIS light illumination. However negative DeNO_x index values under UV-A and extremely low values are achieved under VIS experiments. Although enhancement

of the PHONOS efficiency of fresh P25 due to toluene dosage cannot account for the overall photocatalytic enhancement observed for the NPL/P25 system, it obviously demonstrates some contribution to the observed performance boost.

It is worth noting that in the presence of UV-A and VIS light and water, toluene undergoes partial or total oxidation on the photocatalyst surface. The reaction occurs through two different pathways as shown in Figure 3.21 [85], [86]. $OH^{\bullet}$ radicals may attack to $-CH_3$ functionality (route A) or directly attack to the para position of the aromatic ring due to the presence of electron-donating methyl group (route B). The main intermediates in the photocatalytic degradation of toluene are benzoic acid, benzyl alcohol, and benzaldehyde. It is apparent that for fresh T/P25 samples, in the presence of UV-A or VIS illumination partial oxidation of toluene occurs resulting in the formation of various surface species (such as aromatic oxygenates with -OH, -COH, -COOH, functionalities *etc.*) [85], [86] which may accelerate the NO and NO_2 adsorption. Therefore, facilitated adsorption and increased surface residence times of NO(ads) and NO_2(ads) species on the P25 catalyst surface may boost the oxidative storage of such species and improve PHONOS performance.

On the other hand, upon longer (18 h) UV-A/VIS irradiation of the T/P25 samples, the favorable influence of toluene on P25 PHONOS performance is eliminated due to the saturation of the P25 surface with partial oxidation products or total oxidation of toluene yielding CO_2(ads, g) and H_2O(ads, g).

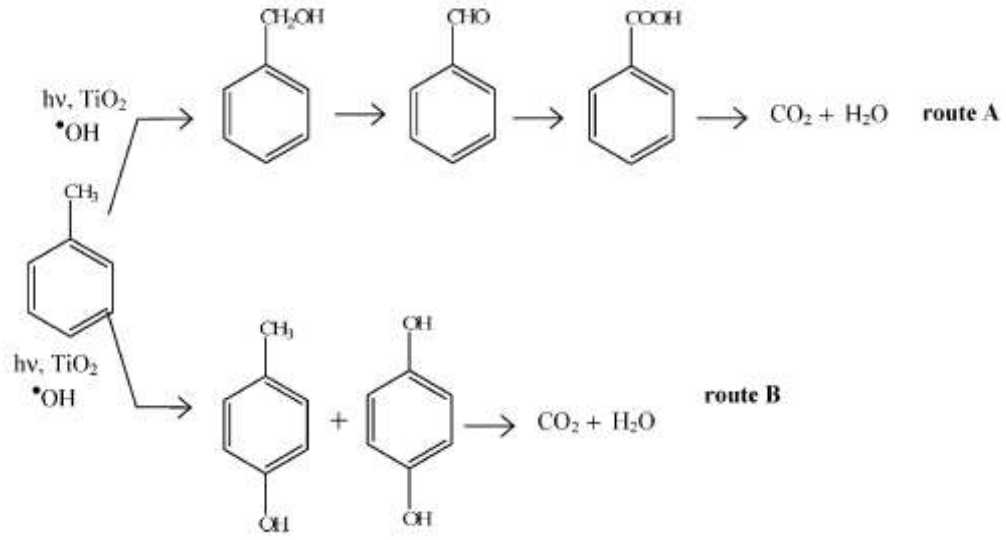

Figure 3.21: Possible route for photocatalytic degradation of toluene [85].

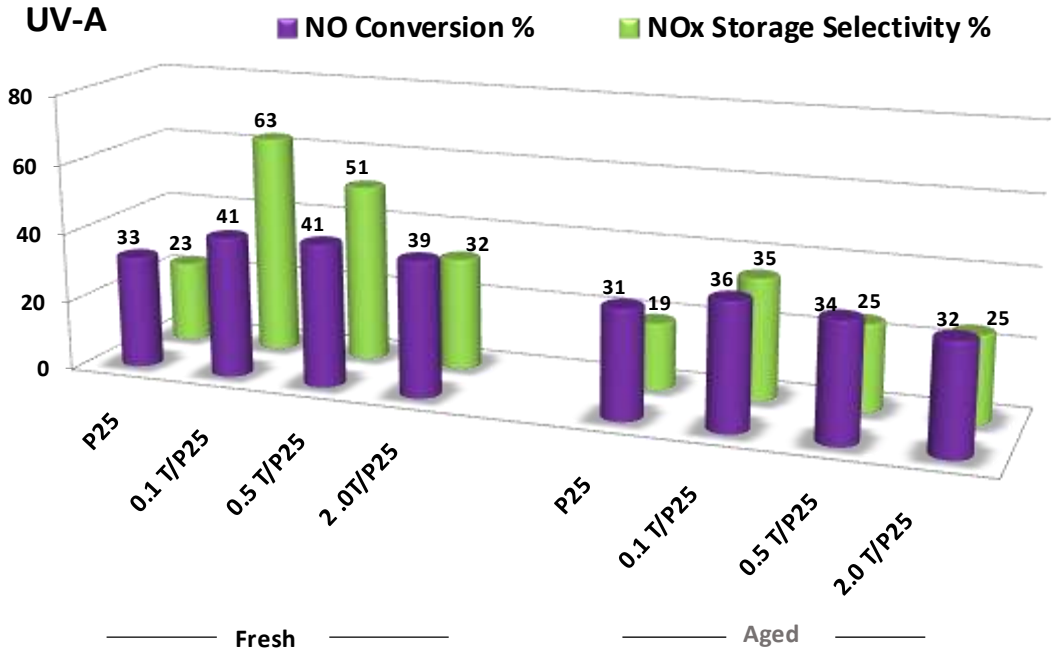

Figure 3.22: % NO(g) conversion and %NO_x storage selectivity values for P25 and T/P25 under UV-A light for fresh and aged samples.

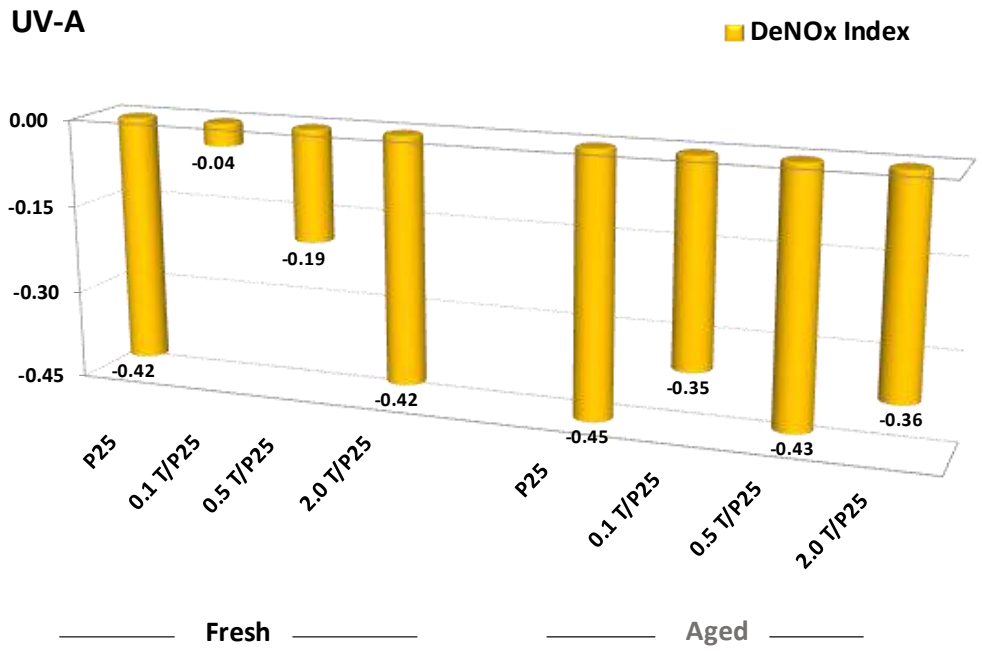

Figure 3.23: DeNO_x index values for P25 and T/P25 under UV-A light for fresh and aged samples.

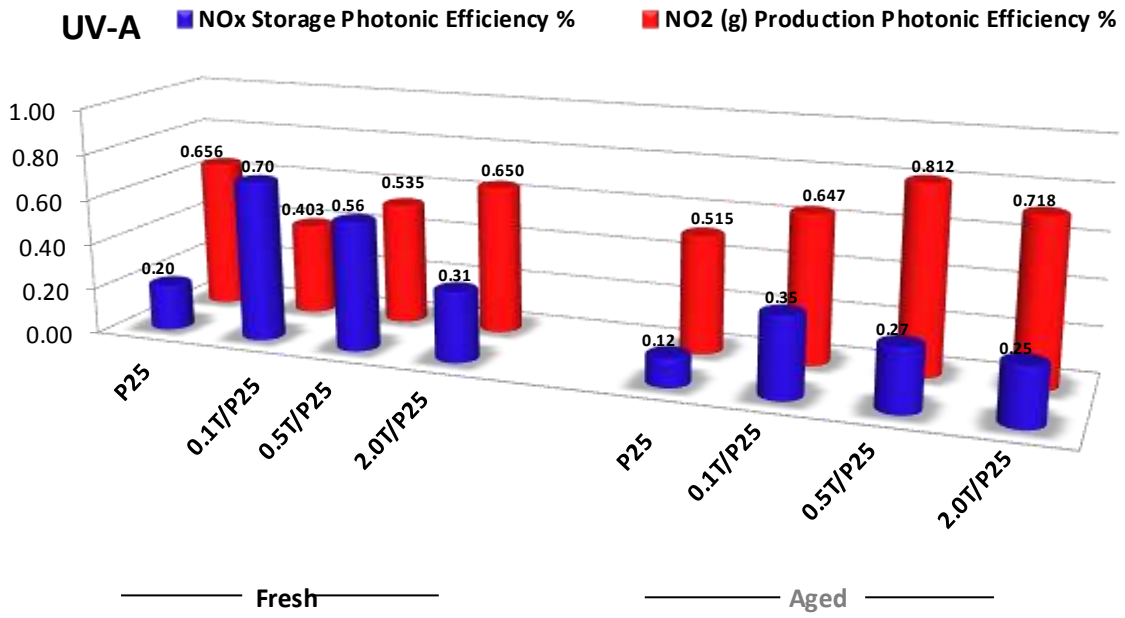

Figure 3.24: % Photonic efficiency values for P25 and T/P25 under VIS light for fresh and aged samples.

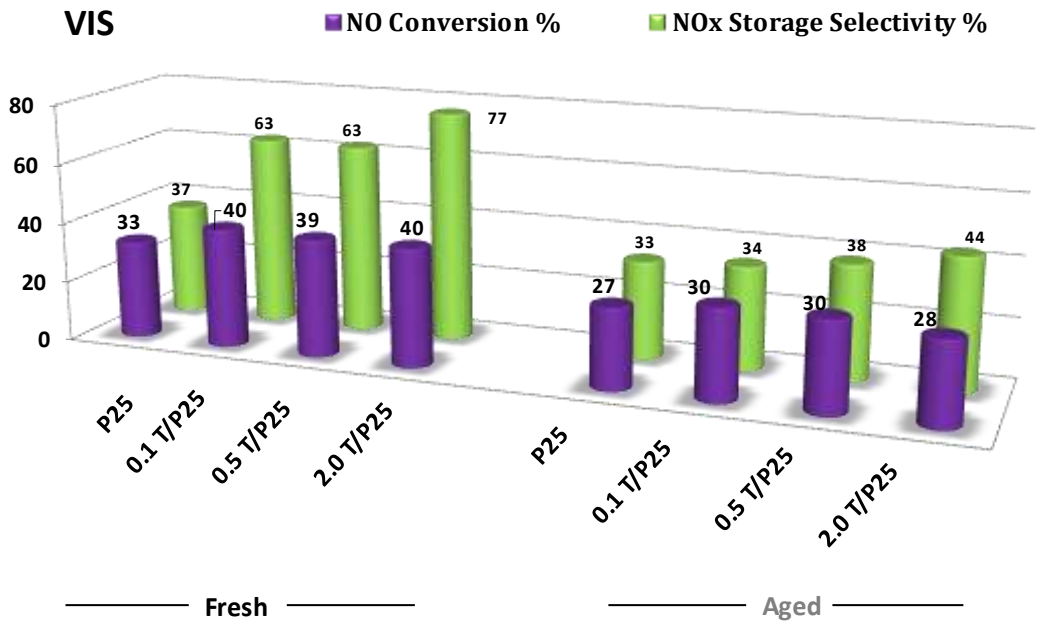

Figure 3.25: % NO(g) conversion and %NOx storage selectivity values for P25 and T/P25 under VIS light for fresh and aged samples.

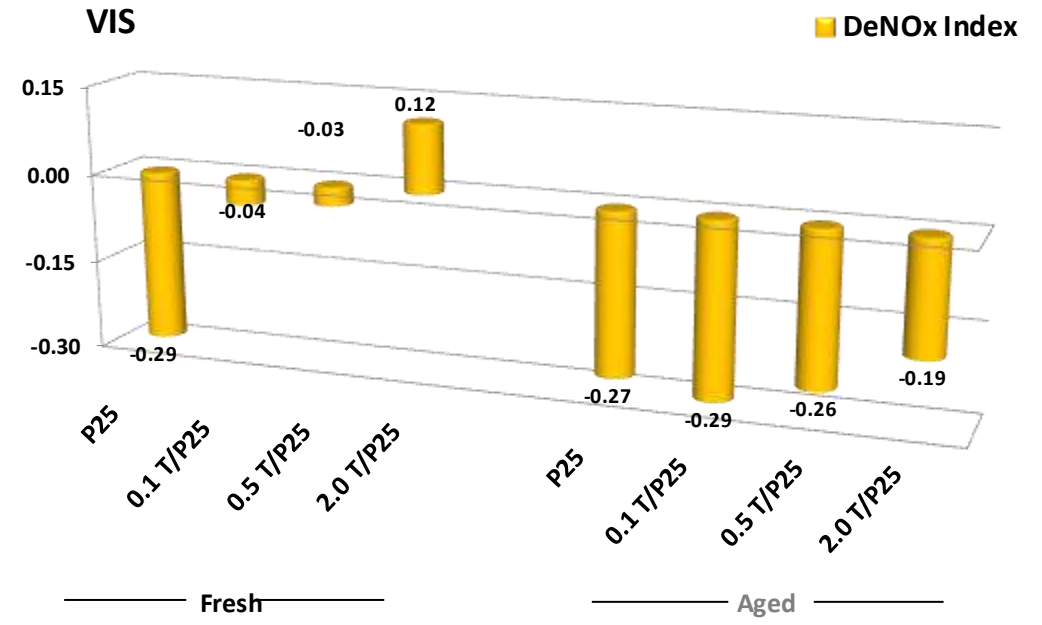

Figure 3.26: DeNO_x index values for P25 and T/P25 under VIS light for fresh and aged samples.

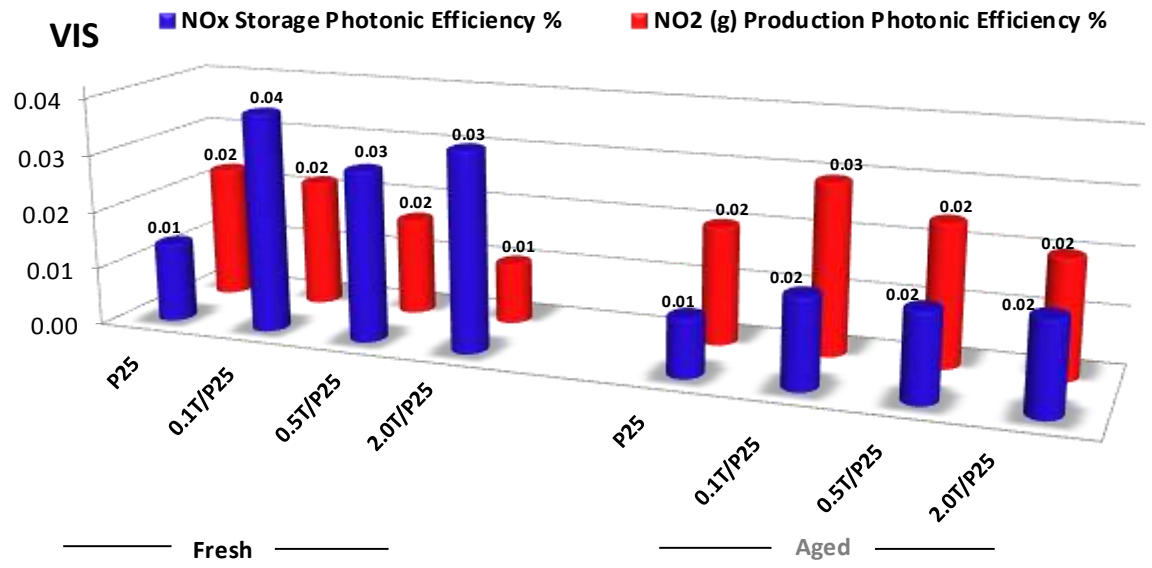

Figure 3.27: % Photonic efficiency values for P25 and T/P25 under VIS light for fresh and aged samples.

3.2.5 Photochemical stability of NPL/P25 composites and reusability

As mentioned before, photocatalytic performance results presented in the previous sections were obtained in 1 h-long experiments. In order to examine the photocatalytic stability/reusability of the NPL/P25 photocatalysts, a series of long-run experiments were performed for P25 as well as for the best performing NPL/P25 catalyst for each illumination type, where, five successive 1 h-long PHONOS tests were carried out under UV-A or VIS-light. For this purpose, PHONOS performance of the following catalyst were tested:

- P25 under UV-A and VIS illumination
- 2.0NPL/P25 under UV-A illumination
- 0.1NPL/P25 under VIS illumination

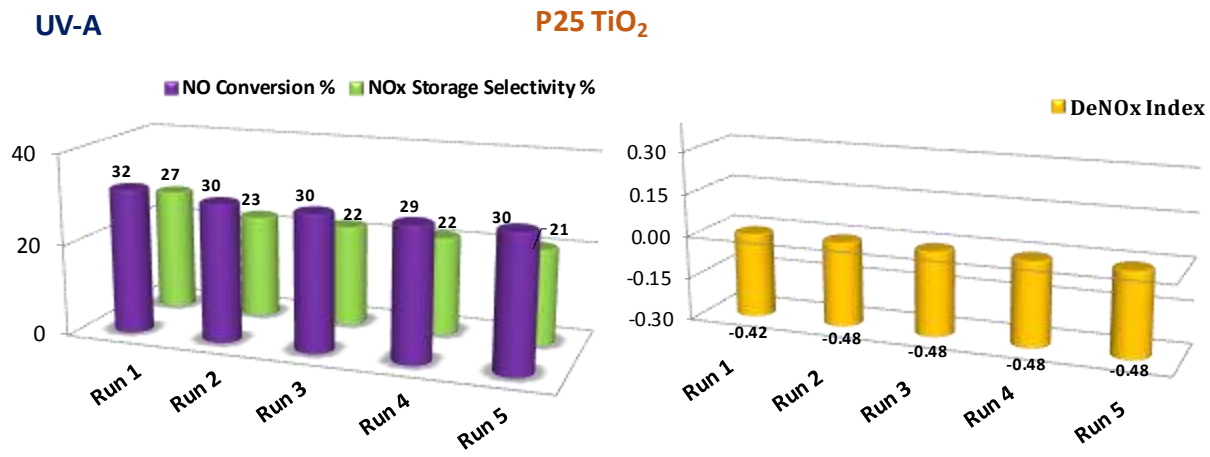

Figure 3.28: Long term photocatalytic results of P25 TiO_2 under UV-A light irradiation.

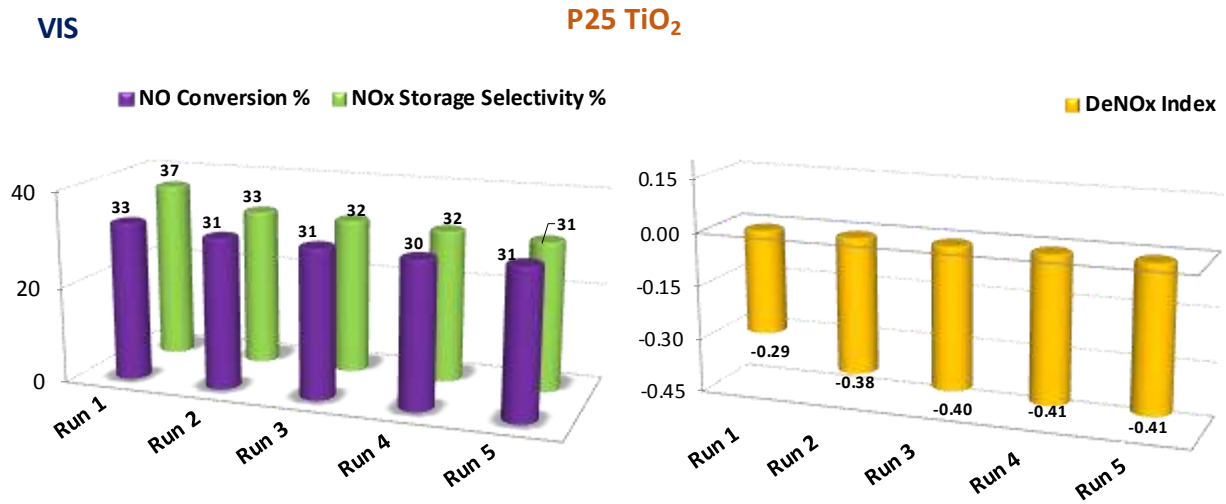

Figure 3.29: Long term photocatalytic results of P25 TiO_2 under VIS light irradiation.

Long term photocatalytic activity of P25 TiO_2 under UV-A as well as VIS irradiation are presented in Figures 3.28 and 3.29. It can be noticed that % NO conversion remains relatively intact after 5 h PHONOS reaction. However, $\%NO_x$ storage selectivity declines which is related to surface saturation of P25 with oxidation products yielding a further decrease in DeNO_x index values in both illumination types. Under UV-A illumination, although initial %NO conversion remained invariant for 2.0 NPL/P25, NO_x storage selectivity decreased from initial value of

93% to 47% after 5 h PHONOS experiment (Figure 3.30.a). Additionally, DeNO_x index values quickly declined to negative values after the second cycle (Figure 3.30.b). This monotonic attenuation in NO_x abatement capability could be probably due to the continuous accumulation of nitrites/nitrates on the photocatalyst surface diminishing the NO_x storage capacity and facilitation of NO_2(g) desorption/release via nitrate reduction.

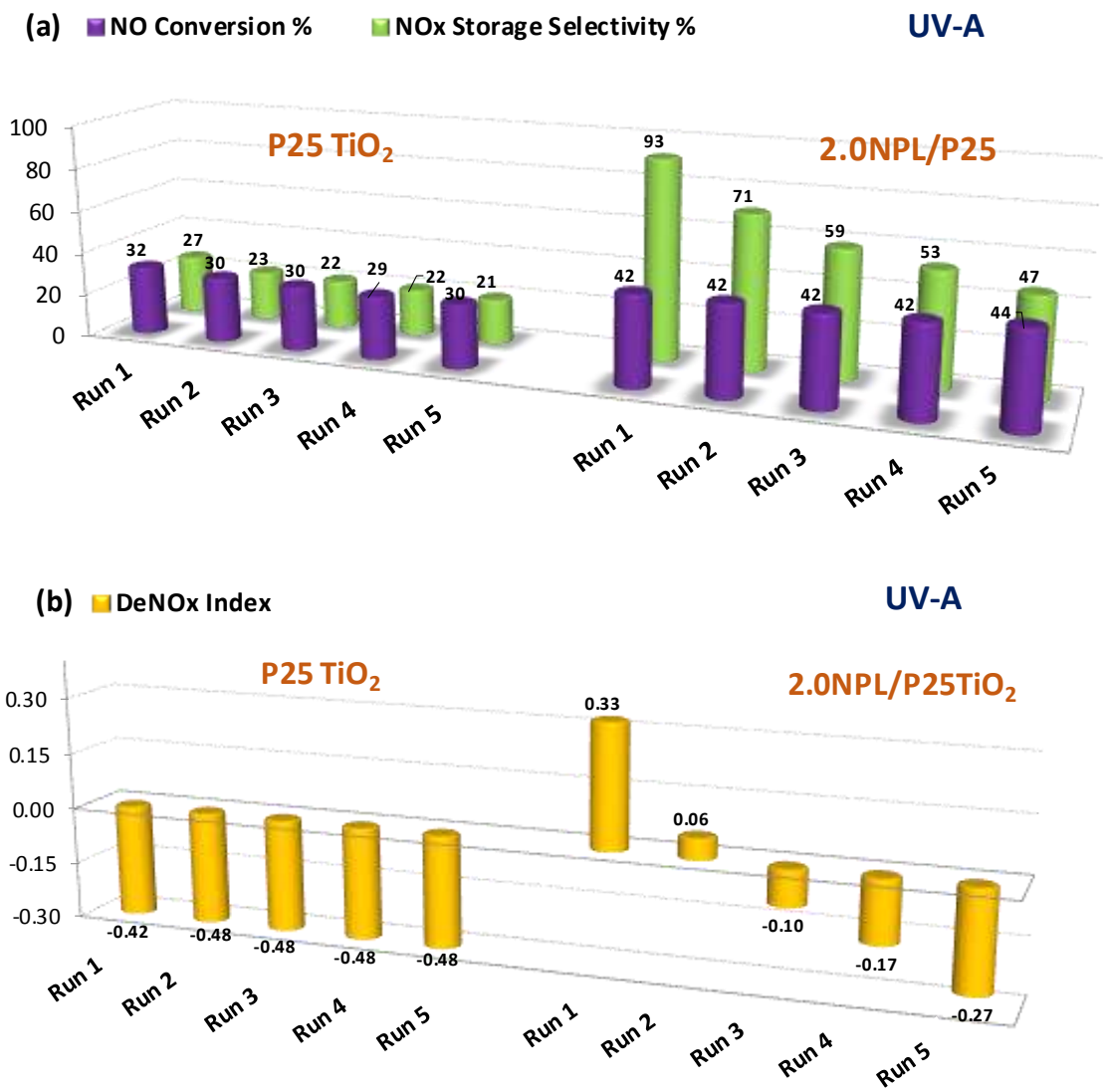

Figure 3.30: Long term %NO conversion, %NO_x storage selectivity and DeNO_x index results of P25 and 2.0NPL/P25 under UV-A light irradiation.

Similarly, under VIS illumination, despite relatively stable %NO conversion for 0.1 NPL/P25 after five runs, initial NO_x Storage Selectivity% (93%) decreased slightly (to 78%), retaining a positive De*NOx* index value after five runs (Figure 3.31). Obtained results suggest that NPL/P25 can store NO_x species even after 5 h which is a considerable advantage compared to pure P25.

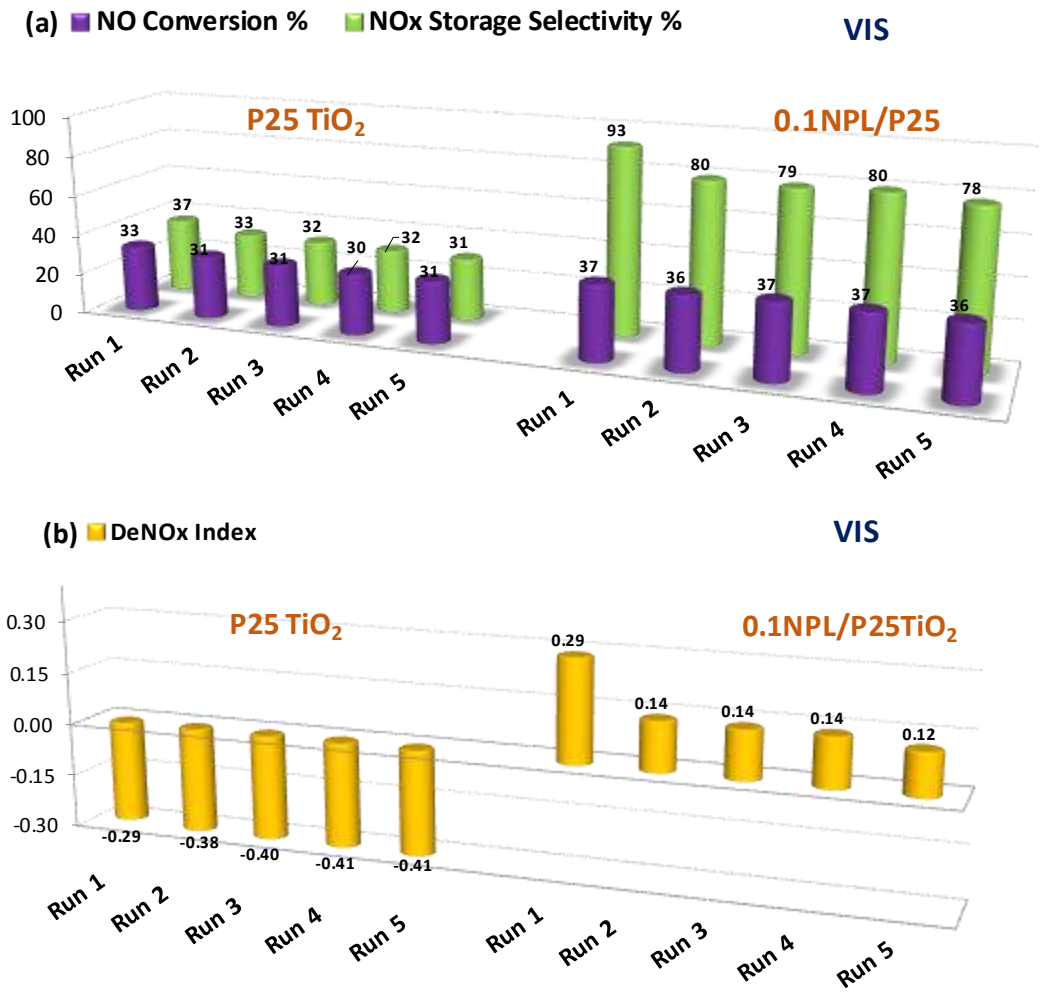

Figure 3.31: (a)Long term %NO conversion, %NO_x storage selectivity and (b) DeNO_x index results of P25 and 0.1 NPL/P25 under VIS light irradiation.

3.2.6 Effect of temperature on photocatalytic performance during VIS irradiation

Control experiments were carried out to understand the effect of temperature during VIS PHONOS experiments. During the UV-A PHONOS tests, the temperature of the reactor remained within 20-25 °C. However, it increased up to 46 °C during VIS light experiments. As mentioned earlier, this is associated with the differences between the emission spectra of the light sources utilized in UV-A and VIS tests. Hence, it is crucial to elucidate the thermal contributions and confirm that the catalytic enhancement observed under VIS light illumination mainly originates from photocatalytic processes and not from thermal catalytic routes. To deal with this issue, temperature of the photocatalytic reactor was changed by adjusting the distance between the VIS-light source and the reactor. VIS photon flux was decreased by increasing the distance between the VIS light source and the reactor, which eventually brought about a drop in the reactor temperature during the PHONOS tests. Then, the photocatalytic performance of the fresh P25 and 0.1 NPL/P25 samples were measured at different reactor temperatures under VIS-light illumination, as demonstrated in Figure 3.32. It is important to highlight that %NO conversion and $\%NO_x$ storage selectivity values rely on the incoming photon flux, therefore they cannot be used to evaluate PHONOS performance of different temperatures at various photon flux values. Thus, % photonic efficiency values are employed in the comparison of the performance data corresponding to different temperatures where NO_x storage and NO_2 generation data were normalized with the incoming photon flux values (Figure 3.32).

These results clearly demonstrate that NO_x storage photonic efficiency% of pure P25 tends to decline with increasing temperature during the VIS-light illumination probably due to accelerated electron-hole recombination or improved water dissociation that is poisoning TiO_2 surface with an extensive amount of adsorbed hydroxyl/hydroxide species. Regarding 0.1NPL/P25 catalyst, while increasing temperature has almost no effect on NO_2 release

photonic efficiency %, it extremely diminishes the NO_x Storage photonic efficiency %, again suggesting a decrease in overall PHONOS performance with increasing temperature. Accordingly, control experiments provided in Figure 3.32 clearly indicate that an increase in the reactor temperature during the VIS-light illumination is not responsible for the observed boost in photocatalytic activity, and the photocatalytic enhancement observed for the NPL/P25 composite system under VIS light is a result of photocatalytic routes rather than conventional thermal catalytic routes.

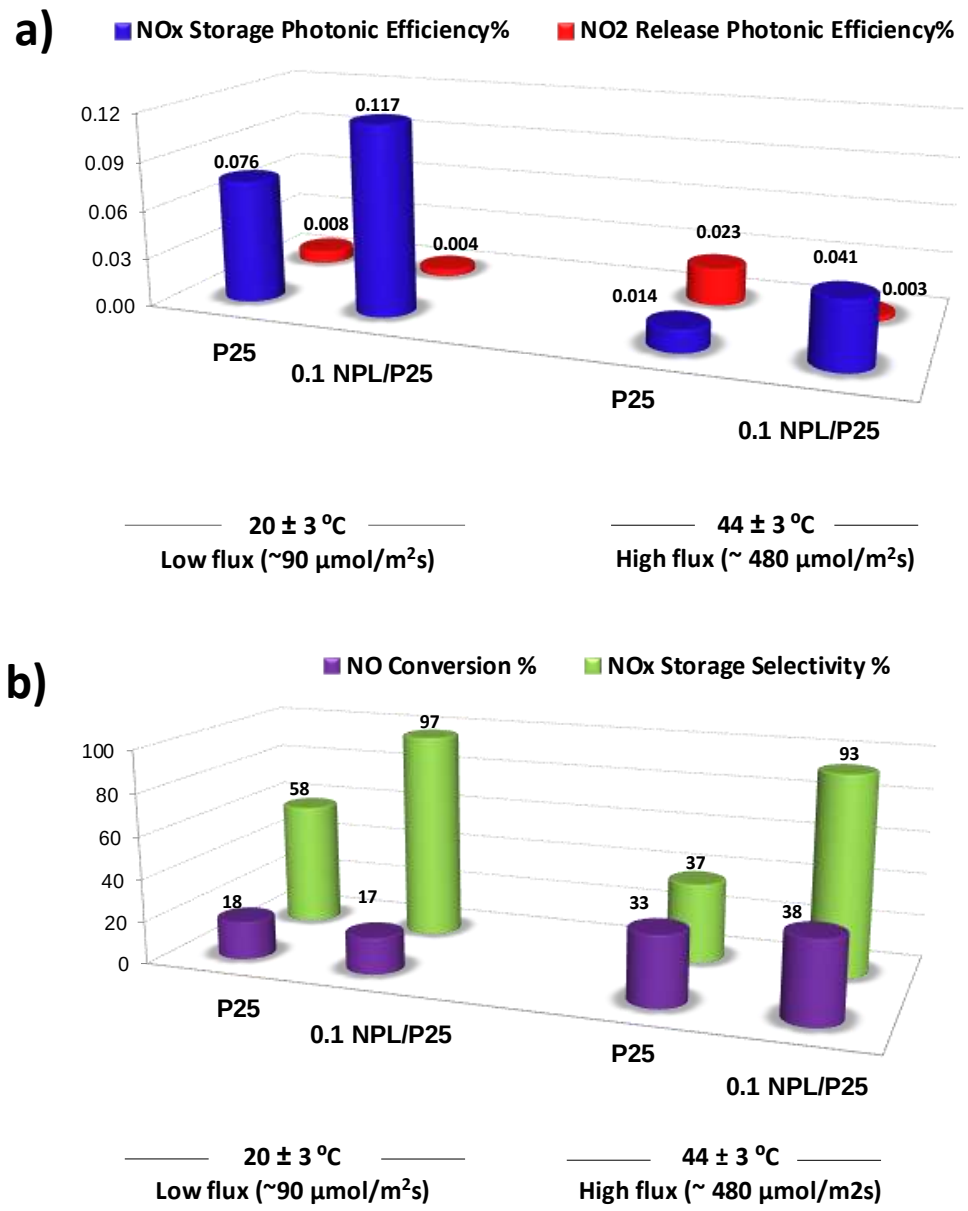

Figure 3.32: Temperature-dependent PHONOS data for pure P25 and 0.1NPL/P25 under VIS-light illumination.

4 Conclusions

In the current study, oleic acid functionalized core/crown CdSe/CdSeTe quantum well nanoplatelets were incorporated onto P25 TiO_2 in an attempt to obtain a broad band NO_x oxidation and storage photocatalyst. Synthesized photocatalysts were tested under both UV and VIS light illumination. NPL/P25 composite photocatalysts with optimized NPL loadings revealed significant photocatalytic NO_x abatement with a relatively high NO(g) conversion and an extremely high selectivity toward NO_x storage compared to commercial P25 TiO_2 both under UV-A and VIS illumination. Roles of the individual components of the NPL/P25 composite were identified through a series of detailed control experiments. These tests suggested that the composite NPL/P25 outperformed the individual components in the catalytic formulation.

It was shown that while primary photocatalytic active sites for NO oxidation reside on titanium dioxide, NPL provided a synergistic boost both in NO conversion as well as NO_x storage selectivity. The origin of the enhanced NO conversion can be attributed to the presumably improved electron-hole separation capability of the utilized colloidal quantum wells. Having a Type-II band alignment, the electron and hole wave functions are conceivably placed in different parts of the NPL heterostructure, resulting in spatial separation of charge carriers and longer fluorescence lifetimes. Moreover, oleic acid functionalities as well as CdSe/CdSeTe core/crown nanoplatelets also facilitated NO_2 adsorption, extended the surface residence time of adsorbed NO_2 species and assisted their conversion to nitrates contributing favorably to the improved photocatalytic activity. Control experiments revealed that toluene which was used as the dispersing medium for NPL also has some contribution to the photocatalytic enhancement and provided a relatively small boost in NO conversion, however,

this effect disappeared upon extended operational times due to the photocatalytic/photochemical degradation of the adsorbed toluene. While reusability was limited under UV-A illumination, NPL/P25 systems displayed reasonable reusability under VIS illumination. Attenuation of the PHONOS performance upon photochemical aging and extended operation can be correlated to electronic changes in the Cd species as well as degradation of the oleic acid capping of the NPL system. (A clear information regarding the oxidation state changes of Te and Se was not achieved due to small NPL loading and overlapping Te and Se signals with other features). Influence of temperature was also studied for the PHONOS performance of NPL/P25 composites under VIS-light suggesting a decrease in photocatalytic efficiency with increasing temperature due to the possible increase in electron-hole recombination rate and the increased formation of hydroxide/hydroxyl surface functionalities poisoning the photocatalyst surface. Similar NPL/P25-based composite systems can be used as a new family of active photocatalytic materials with a significant potential in various environmental remediation and solar energy conversion applications.

Appendix

Synthesis of CdSe (core)/CdSeTe (crown) nanoplatelets

Preparation of Cadmium Myristate

Cadmium myristate ($C_{28}H_{54}CdO_4$, Cd(II)tetradecanoate) was prepared according to the protocol reported in literature [54]. Briefly, 6.26 g of sodium myristate and 2.46 g of cadmium nitrate tetrahydrate were separately dissolved in 500 and 80 mL of methanol, respectively. After complete dissolution, the achieved solutions were mixed and stirred vigorously for 3 h. Consequently, the white cadmium myristate powder was precipitated by centrifugation and washed with methanol three times to remove any unwanted impurities and/or side products. Lastly, cadmium myristate was dried overnight under vacuum at room temperature (RT).

Synthesis of the 4 ML-thick CdSe core of NPL

CdSe core of NPL with four-monolayer thickness (*i.e.* consisting of four Se atomic layers and five Cd atomic layers) were synthesized by using the same procedure in the previous section. 20 mg of Se, 340 mg of cadmium myristate (synthesized in previous step) and 30 mL of 1-octadecene were placed in a 100 mL three-neck flask and degassed at 95 °C for 1 h to remove oxygen, water and any other volatile species. Next, the sample temperature was increased under the Ar(g) flow. At *ca.* 195 °C, the color of the reaction solution turned golden yellow, after which, 120 mg of $Cd(OAc)_2{\cdot}2H_2O$ was promptly added to the reaction system. After having kept the reaction solution at 240 °C for 8 min for further growth of NPL, 1 mL of oleic acid was injected. At this point, reaction was stopped, and the temperature of the solution was brought to RT. Subsequently, hexane (10 mL) and ethanol (10 mL) were added to the

solution to precipitate the synthesized NPL. Lastly, NPL were centrifuged and stored in hexane for the crown coating step.

Synthesis of the 4 ML-Thick CdSe/$CdSe_{0.75}Te_{0.25}$ Core/Alloyed Crown

In this step, 2 mL of 4 ML-thick CdSe core suspension in hexane (where 0.1 mL of this suspension in 3 mL of hexane had an optical density of 0.9 at 512 nm), 10 mL of 1-octadecene, 100 µL of oleic acid and 50 mg of cadmium acetate dihydrate were combined in a 25 mL three-neck round bottom flask. The reaction mixture was degassed at RT for 1 h and then was set to 215 °C under Ar(g) flow for the growth of the CdTe crown region. At 185 °C, 0.75 mL of ODE−TOP-Se-Te solution was injected to the reaction medium at a rate of 2.5 mL/h (where ODE−TOP-Se-Te solution was prepared by mixing 79 mg Se and 127.6 mg Te with 2 mL of TOP in an inert atmosphere overnight to ensure complete dissolution. Next, 60 µL of this mixture was diluted with 2 ml of ODE to achieve the final ODE−TOP-Se-Te solution). It is important to note here that if needed, the size of the crown region could be controlled by varying the amount of the injected ODE−TOP-Se-Te solution. Immediately after the injection of ODE-TOP-Se-Te solution, 1 mL of oleic acid was swiftly added to the reaction medium and the solution was quenched to RT. CdSe/$CdSe_{0.75}Te_{0.25}$ Core/Alloyed Crown NPL were precipitated by the addition of ethanol, centrifuged and finally dispersed in toluene for further studies [65].

References

[1] J. Patzsch, J. N. Spencer, A. Folli, and J. Z. Bloh, "Grafted iron(iii) ions significantly enhance NO_2 oxidation rate and selectivity of TiO_2 for photocatalytic NO_x abatement," *RSC Adv.*, vol. 8, no. 49, pp. 27674–27685, 2018.

[2] Criteria Air Pollutants, "United States Environmental Protection Agency," *Accessed: July 2020*. [Online]. Available: https://www.epa.gov/criteria-air-pollutants.

[3] J. Ângelo, L. Andrade, L. M. Madeira, and A. Mendes, "An overview of photocatalysis phenomena applied to NO_x abatement," *J. Environ. Manage.*, vol. 129, pp. 522–539, 2013.

[4] A. Folli, S. B. Campbell, J. A. Anderson, and D. E. MacPhee, "Role of TiO_2 surface hydration on NO oxidation photo-activity," *J. Photochem. Photobiol. A Chem.*, vol. 220, no. 2–3, pp. 85–93, 2011.

[5] Environmental Protection Agency (EPA), "Nitrogen oxides (NO_x), why and how they are controlled," *Epa-456/F-99-006R*, p. 48, 1999.

[6] K. Skalska, J. S. Miller, and S. Ledakowicz, "Trends in NO_x abatement: A review," *Sci. Total Environ.*, vol. 408, no. 19, pp. 3976–3989, 2010.

[7] J. Lelieveld and F. J. Dentener, "What controls tropospheric ozone?," *J. Geophys. Res. Atmos.*, vol. 105, pp. 3531–3551, 2000.

[8] B. C. Baukal, "Everything You Need to Know About NO_x," *Met. Finish.*, vol. 103, no. 11, pp. 18–24, 2015.

[9] H. Zhao, S. Wang, W. Wang, R. Liu, and B. Zhou, "Investigation of ground-level ozone and high-pollution episodes in a megacity of eastern China," *PLoS One*, vol. 10, no. 6, pp. 1–20, 2015.

[10] J. J. Zhang, Y. Wei, and Z. Fang, "Ozone pollution: A major health hazard worldwide," *Front. Immunol.*, vol. 10, pp. 1–10, 2019.

[11] F. A. B. Abdul Aziz, N. Rahman, and J. Mohd Ali, "Tropospheric ozone formation estimation in Urban City, Bangi, Using Artificial Neural Network (ANN)," *Comput. Intell. Neurosci.*, 2019. https://doi.org/10.1155/2019/6252983

[12] J. A. Driscoll and R. F. Jones, "Acid rain demonstration: The formation of nitrogen oxides as a by-product of high-temperature flames in connection with internal combustion engines," *J. Chem. Educ.*, vol. 74, no. 12, pp. 1424–1425, 1997.

[13] A. J. Haagen-Smit, "Chemistry and Physiology of Los Angeles Smog," *Ind. Eng. Chem.*, vol. 44, no. 6, pp. 1342–1346, 1952.

[14] "Sector share of nitrogen oxides emissions," "European Environment Agency." [Online]. Available: https://www.eea.europa.eu/data-and-maps/indicators/eea-32-nitrogen-oxides-NO_x-emissions-1/assessment.2010-08-19.0140149032-3.

[15] S. Saravanan, G. Nagarajan, S. Anand, and S. Sampath, "Correlation for thermal NO_x formation in compression ignition (CI) engine fuelled with diesel and biodiesel," *Energy*, vol. 42, no. 1, pp. 401–410, 2012.

[16] A. A. Nizami and N. P. Cernansky, "NO_x formation in monodisperse fuel spray combustion," *Proc. Seventeenth Symposium (Intl.)Combust.*, vol. 17, no. 1, pp. 475–483, 1979.

[17] J. Lasek, Y. H. Yu, and J. C. S. Wu, "Removal of NO_x by photocatalytic processes," *J. Photochem. Photobiol. C Photochem. Rev.*, vol. 14, no. 1, pp. 29–52, 2013.

[18] M. Irfan, M. Sevim, Y. Koçak, M. Balci, Ö. Metin, and E. Özensoy, "Enhanced photocatalytic NO_x oxidation and storage under visible-light irradiation by anchoring Fe_3O_4 nanoparticles on mesoporous graphitic carbon nitride (mpg-C_3N_4)," *Appl. Catal. B Environ.*, vol. 249, pp. 126–137, 2019.

[19] T. V. W. Janssens *et al.*, "A consistent reaction scheme for the selective catalytic reduction of nitrogen oxides with ammonia," *ACS Catal.*, vol. 5, no. 5, pp. 2832–2845, 2015.

[20] G. Busca, L. Lietti, G. Ramis, and F. Berti, "Chemical and mechanistic aspects of the selective catalytic reduction of $NO_{(x)}$ by ammonia over oxide catalysts: A review," *Appl. Catal. B Environ.*, vol. 18, no. 1–2, pp. 1–36, 1998.

[21] S. Andonova, Z. A. Ok, N. Drenchev, E. Özensoy, and K. Hadjiivanov, "Pt/CeO_x/ZrO_x/γ-Al_2O_3 Ternary Mixed Oxide DeNO_x Catalyst: Surface Chemistry and NO_x Interactions," *J. Phys. Chem. C*, vol. 122, no. 24, pp. 12850–12863, 2018.

[22] S. Matsumoto, Y. Ikeda, H. Suzuki, M. Ogai, and N. Miyoshi, "$NO_{(x)}$ storage-reduction catalyst for automotive exhaust with improved tolerance against sulfur poisoning," *Appl. Catal. B Environ.*, vol. 25, no. 2–3, pp. 115–124, 2000.

[23] A. Bueno-López, D. Lozano-Castelló, and J. A. Anderson, "NO_x storage and reduction over copper-based catalysts. Part 1: BaO + CeO_2 supports," *Appl. Catal. B Environ.*, vol. 198, pp. 189–199, 2016.

[24] H. P. Nguyen, S. Palma Del Valle, and O. Marie, "NO_x adsorption on K and Ba loaded on zirconia-titania NSR catalysts: A comparative study by in situ and operando IR spectroscopy," *Appl. Catal. B Environ.*, vol. 231, pp. 391–399, 2018.

[25] W. S. Epling, L. E. Campbell, A. Yezerets, N. W. Currier, and J. E. Parks, "Overview of the fundamental reactions and degradation mechanisms of NO_x storage/reduction catalysts," *Catal. Rev. - Sci. Eng.*, vol. 46, no. 2, pp. 163–245, 2004.

[26] M. Happel, A. Desikusumastuti, M. Sobota, M. Laurin, and J. Libuda, "Impact of sulfur poisoning on the NO_x uptake of a NO_x storage and reduction (NSR) model catalyst," *J. Phys. Chem. C*, vol. 114, no. 10, pp. 4568–4575, 2010.

[27] J. C. Schlatter and P. J. Mitchell, "Three-Way Catalyst Response to Transients," *Ind. Eng. Chem. Prod. Res. Dev.*, vol. 19, no. 3, pp. 288–293, 1980.

[28] F. Parrino, C. De Pasquale, and L. Palmisano, "Influence of Surface-Related Phenomena on Mechanism, Selectivity, and Conversion of TiO_2 -Induced Photocatalytic Reactions," *ChemSusChem*, vol. 12, no. 3. pp. 589–602, 2019.

[29] M. Balci Leinen, D. Dede, M. U. Khan, Y. Koçak, H. V. Demir, and E. Özensoy, "CdTe Quantum Dot-Functionalized P25 Titania Composite with Enhanced Photocatalytic NO_2 Storage Selectivity under UV and Vis Irradiation," *ACS Appl. Mater. Interfaces*, vol. 11, no. 1, pp. 865–879, 2019.

[30] K. Fujiwara and S. E. Pratsinis, "Single Pd atoms on TiO_2 dominate photocatalytic NO_x removal," *Appl. Catal. B Environ.*, vol. 226, pp. 127–134, 2018.

[31] M. Çağlayan, M. Irfan, K. E. Ercan, Y. Koçak, and E. Özensoy, "Enhancement of photocatalytic NO_x abatement on titania via additional metal oxide NO_x-storage domains: Interplay between surface acidity, specific surface area, and humidity," *Appl.*

Catal. B Environ., vol. 263, p. 118227, 2020.

[32] J. Ângelo, L. Andrade, and A. Mendes, "General Highly active photocatalytic paint for NO_x abatement under real-outdoor conditions," *"Applied Catal. A, Gen.*, vol. 484, pp. 17–25, 2014.

[33] R. Sugrañez *et al.*, "Enhanced photocatalytic degradation of NO_x gases by regulating the microstructure of mortar cement modified with titanium dioxide," *Build. Environ.*, vol. 69, pp. 55–63, 2013.

[34] L. Yang, A. Hakki, F. Wang, and D. E. Macphee, "Different Roles of Water in Photocatalytic $DeNO_x$ Mechanisms on TiO_2: Basis for Engineering Nitrate Selectivity?," *ACS Appl. Mater. Interfaces*, vol. 9, no. 20, pp. 17034–17041, 2017.

[35] R. Dillert, A. Engel, J. Große, P. Lindner, and D. W. Bahnemann, "Light intensity dependence of the kinetics of the photocatalytic oxidation of nitrogen(ii) oxide at the surface of TiO_2," *Phys. Chem. Chem. Phys.*, vol. 15, no. 48, pp. 20876–20886, 2013.

[36] L. Sivachandiran, F. Thevenet, P. Gravejat, and A. Rousseau, "Investigation of NO and NO_2 adsorption mechanisms on TiO_2 at room temperature," *Appl. Catal. B Environ.*, vol. 142–143, no. 2, pp. 196–204, 2013.

[37] M. A. Henderson, "A surface science perspective on TiO_2 photocatalysis," *Surf. Sci. Rep.*, vol. 66, no. 6–7, pp. 185–297, 2011.

[38] J. Freitag *et al.*, "Nitrogen(II) oxide charge transfer complexes on TiO_2: A new source for visible-light activity," *J. Phys. Chem. C*, vol. 119, no. 9, pp. 4488–4501, 2015.

[39] Y. Ohko, Y. Nakamura, N. Negishi, S. Matsuzawa, and K. Takeuchi, "Unexpected release of HNO_3 and related species from UV-illuminated TiO_2 surface into air in photocatalytic oxidation of NO_2," *Environ. Chem. Lett.*, vol. 8, no. 3, pp. 289–294, 2010.

[40] Y. Ohko, Y. Nakamura, N. Negishi, S. Matsuzawa, and K. Takeuchi, "Photocatalytic oxidation of nitrogen monoxide using TiO_2 thin films under continuous UV light illumination," *J. Photochem. Photobiol. A Chem.*, vol. 205, no. 1, pp. 28–33, 2009.

[41] J. Zhang, P. Zhou, J. Liu, and J. Yu, "New understanding of the difference of photocatalytic activity among anatase, rutile and brookite TiO_2," *Phys. Chem. Chem. Phys.*, vol. 16, no. 38, pp. 20382–20386, 2014.

[42] H. Chen, C. E. Nanayakkara, and V. H. Grassian, "Titanium dioxide photocatalysis in atmospheric chemistry," *Chem. Rev.*, vol. 112, no. 11, pp. 5919–5948, 2012.

[43] D. A. H. Hanaor and C. C. Sorrell, "Review of the anatase to rutile phase transformation," *Journal of Materials Science*, vol. 46, no. 4. pp. 855–874, 2011.

[44] D. Reyes-Coronado, G. Rodríguez-Gattorno, M. E. Espinosa-Pesqueira, C. Cab, R. De Coss, and G. Oskam, "Phase-pure TiO_2 nanoparticles: Anatase, brookite and rutile," *Nanotechnology*, vol. 19, no. 14, p. 145605, 2008.

[45] K. Ozawa *et al.*, "Electron-hole recombination time at TiO_2 single-crystal surfaces: Influence of surface band bending," *J. Phys. Chem. Lett.*, vol. 5, no. 11, pp. 1953–1957, 2014.

[46] N. O. Balayeva, M. Fleisch, and D. W. Bahnemann, "Surface-grafted WO_3/TiO_2 photocatalysts: Enhanced visible-light activity towards indoor air purification," *Catal. Today*, vol. 313, pp. 63–71, 2018.

[47] S. Jafari, M. R. Mohammadi, and H. R. Madaah Hosseini, "Impact of morphology and nitrogen and carbon codoping on photocatalytic activity of TiO_2 as environmental catalysts," *Ind. Eng. Chem. Res.*, vol. 55, no. 47, pp. 12205–12212, 2016.

[48] Q. L. Yu, M. M. Ballari, and H. J. H. Brouwers, "Indoor air purification using heterogeneous photocatalytic oxidation. Part II: Kinetic study," *Appl. Catal. B Environ.*, vol. 99, no. 1–2, pp. 58–65, 2010.

[49] A. Yeltik, S. Delikanli, M. Olutas, Y. Kelestemur, B. Guzelturk, and H. V. Demir, "Experimental Determination of the Absorption Cross-Section and Molar Extinction Coefficient of Colloidal CdSe Nanoplatelets," *J. Phys. Chem. C*, vol. 119, no. 47, pp. 26768–26775, 2015.

[50] T. Edvinsson, "Optical quantum confinement and photocatalytic properties in two-, one- and zero-dimensional nanostructures," *R. Soc. Open Sci.*, vol. 5, no. 9, p. 180387, 2018.

[51] A. C. Berends and C. De Mello Donega, "Ultrathin One- and Two-Dimensional Colloidal Semiconductor Nanocrystals: Pushing Quantum Confinement to the Limit," *J. Phys. Chem. Lett.*, vol. 8, no. 17, pp. 4077–4090, 2017.

[52] B. T. Diroll, "Colloidal quantum wells for optoelectronic devices," *J. Mater. Chem. C*,

2020. DOI: 10.1039/d0tc01164a

[53] S. Pedetti *et al.*, "Optimized synthesis of CdTe nanoplatelets and photoresponse of CdTe nanoplatelets films," *Chem. Mater.*, vol. 25, no. 12, pp. 2455–2462, 2013.

[54] M. D. Tessier, P. Spinicelli, D. Dupont, G. Patriarche, S. Ithurria, and B. Dubertret, "Efficient exciton concentrators built from colloidal core/crown CdSe/CdS semiconductor nanoplatelets," *Nano Lett.*, vol. 14, no. 1, pp. 207–213, 2014.

[55] B. Mahler, B. Nadal, C. Bouet, G. Patriarche, and B. Dubertret, "Core/shell colloidal semiconductor nanoplatelets," *J. Am. Chem. Soc.*, vol. 134, no. 45, pp. 18591–18598, 2012.

[56] Y. Kelestemur, B. Guzelturk, O. Erdem, M. Olutas, K. Gungor, and H. V. Demir, "Platelet-in-Box Colloidal Quantum Wells: CdSe/CdS@CdS Core/Crown@Shell Heteronanoplatelets," *Adv. Funct. Mater.*, vol. 26, no. 21, pp. 3570–3579, 2016.

[57] M. Sharma, S. Delikanli, and H. V. Demir, "Two-Dimensional CdSe-Based Nanoplatelets: Their Heterostructures, Doping, Photophysical Properties, and Applications," *Proc. IEEE*, vol. 108, no. 5, pp. 1–21, 2019.

[58] S. Ithurria and D. V Talapin, "Colloidal Atomic Layer Deposition (c-ALD) using Self-Limiting Reactions at Nanocrystal Surface Coupled to Phase Transfer between Polar and Nonpolar Media," *J. Am. Chem. Soc.*, vol. 134, pp. 18585−18590, 2012.

[59] K. Boldt, N. Kirkwood, G. A. Beane, and P. Mulvaney, "Synthesis of Highly Luminescent and Photo-Stable, Graded Shell CdSe/$Cd_xZn_{1-x}S$ Nanoparticles by In Situ Alloying," *Chem. Mater.*, vol. 25, no. 23, pp. 4731−4738, 2013.

[60] A. Prudnikau, A. Chuvilin, and M. Artemyev, "CdSe−CdS Nanoheteroplatelets with Efficient Photoexcitation of Central CdSe Region through Epitaxially Grown CdS Wings," *J. Am. Chem. Soc.*, vol. 135, no. 39, pp. 14476–14479, 2013.

[61] C. Nanoplatelets, B. Guzelturk, Y. Kelestemur, M. Olutas, S. Delikanli, and H. V. Demir, "Amplified Spontaneous Emission and Lasing in Colloidal Nanoplatelets," *ACS Nano*, vol. 8, no. 7, pp. 6599–6605, 2014.

[62] T. K. Kormilina, S. A. Cherevkov, A. V. Fedorov, and A. V. Baranov, "Cadmium Chalcogenide Nano-Heteroplatelets: Creating Advanced Nanostructured Materials by

Shell Growth, Substitution, and Attachment," *Small,* vol. 13, no. 41, p. 1702300, 2017.

[63] I. Fedin and D. V. Talapin, "Colloidal CdSe Quantum Rings," *J. Am. Chem. Soc.*, vol. 138, no. 31, pp. 9771–9774, 2016.

[64] Y. Kelestemur *et al.*, "CdSe/$CdSe_{1-x}Te_x$ Core/Crown Heteronanoplatelets: Tuning the Excitonic Properties without Changing the Thickness," *J. Phys. Chem. C*, vol. 121, no. 8, pp. 4650–4658, 2017.

[65] Y. Kelestemur, M. Olutas, S. Delikanli, B. Guzelturk, M. Z. Akgul, and H. V. Demir, "Type-II colloidal quantum wells: CdSe/CdTe core/crown heteronanoplatelets," *J. Phys. Chem. C*, vol. 119, no. 4, pp. 2177–2185, 2015.

[66] J. S. Dalton, P. Janes, N. Jones, K. R. Hallam, J. A. Nicholson, and G. C. Allen, "Photocatalytic oxidation of NO_x gases using TiO_2: A surface spectroscopic approach," *Environ. Pollut.*, vol. 120, no. 2, pp. 415–422, 2002.

[67] Y. Gao *et al.*, "Low-threshold lasing from colloidal CdSe/CdSeTe core/alloyed-crown type-II heteronanoplatelets," *Nanoscale*, vol. 10, no. 20, pp. 9466–9475, 2018.

[68] S. Pedetti, S. Ithurria, H. Heuclin, G. Patriarche, and B. Dubertret, "Type-II CdSe/CdTe core/crown semiconductor nanoplatelets," *J. Am. Chem. Soc.*, vol. 136, no. 46, pp. 16430–16438, 2014.

[69] W. R. G. Baeyens *et al.*, "Chemiluminescence-based detection: Principles and analytical applications in flowing streams and in immunoassays," *J. Pharm. Biomed. Anal.*, vol. 17, no. 6–7, pp. 941–953, 1998.

[70] B. Practice, C. Rates, and A. Q. Yields, "Best Practice in Photocatalysis : Comparing Rates or Apparent quantum yields?," J. *Phys. Chem. Lett.*, vol. 6, no. 10, pp. 1907−1910, 2015.

[71] A. A. Mosquera *et al.*, "Exciton and core-level electron confinement effects in transparent ZnO thin films," *Sci. Rep.*, vol. 3, no. 1, pp. 1–7, 2013.

[72] H. S. White, A. J. Ricco, and M. S. Wrighton, "Characterization of p-type CdTe electrodes in acetonitrile/electrolyte solutions. Nearly ideal behavior from reductive surface pretreatments," *J. Phys. Chem.*, vol. 87, no. 25, pp. 5140–5150, 1983.

[73] G. R. Bhand and N. B. Chaure, "Synthesis of CdTe, CdSe and CdTe/CdSe core/shell

QDs from wet chemical colloidal method," *Mater. Sci. Semicond. Process.*, vol. 68, pp. 279–287, 2017.

[74] A. P. Kumar *et al.*, "Novel dithiols as capping ligands for CdSe quantum dots: Optical properties and solar cell applications," *J. Mater. Chem. C*, vol. 3, no. 9, pp. 1957–1964, 2015.

[75] S. Bourgeois, P. le Seigneur, and M. Perdereau, "Study by XPS of ultra-thin nickel deposits on TiO_2(100) supports with different stoichiometries," *Surf. Sci.*, vol. 328, no. 1–2, pp. 105–110, 1995.

[76] M. N. Ghazzal, R. Wojcieszak, G. Raj, and E. M. Gaigneaux, "Study of mesoporous CdS-quantum-dot-sensitized TiO_2 films by using x-ray photoelectron spectroscopy and afm," *Beilstein J. Nanotechnol.*, vol. 5, no. 1, pp. 68–76, 2014.

[77] B. Guzelturk, Y. Kelestemur, M. Olutas, Q. Li, T. Lian, and H. V. Demir, "High-Efficiency Optical Gain in Type-II Semiconductor Nanocrystals of Alloyed Colloidal Quantum Wells," *J. Phys. Chem. Lett.*, vol. 8, no. 21, pp. 5317–5324, 2017.

[78] D. Dede *et al.*, "Highly Stable Multicrown Heterostructures of Type-II Nanoplatelets for Ultralow Threshold Optical Gain," *Chem. Mater.*, vol. 31, no. 5, pp. 1818–1826, 2019.

[79] D. Karimian, B. Yadollahi, and V. Mirkhani, "Harvesting visible light for aerobic oxidation of alcohols by a novel and efficient hybrid polyoxometalate," *Dalt. Trans.*, vol. 44, no. 4, pp. 1709–1715, 2015.

[80] A. S. Hassanien and A. A. Akl, "Effect of Se addition on optical and electrical properties of chalcogenide CdSSe thin films," *Superlattices Microstruct.*, vol. 89, pp. 153–169, 2016.

[81] H. T. Tung, D. Van Thuan, J. H. Kiat, and D. H. Phuc, "Ag^+ ion doped on the CdSe quantum dots for quantum-dot-sensitized solar cells' application," *Appl. Phys. A Mater. Sci. Process.*, vol. 125, no. 8, pp. 1–9, 2019.

[82] O. I. Mićić, A. J. Nozik, E. Lifshitz, T. Rajh, O. G. Poluektov, and M. C. Thurnauer, "Electron and hole adducts formed in illuminated InP colloidal quantum dots studied by electron paramagnetic resonance," *J. Phys. Chem. B*, vol. 106, no. 17, pp. 4390–4395, 2002.

[83] L. Sivachandiran, F. Thevenet, P. Gravejat, and A. Rousseau, "Investigation of NO and NO_2 adsorption mechanisms on TiO_2 at room temperature," *Appl. Catal. B Environ.*, vol. 142–143, no. 2, pp. 196–204, 2013.

[84] J. Rathouský, V. Kalousek, M. Kolář, J. Jirkovský, and P. Barták, "A study into the self-cleaning surface properties - The photocatalytic decomposition of oleic acid," *Catal. Today*, vol. 161, no. 1, pp. 202–208, 2011.

[85] S. Ardizzone, C. L. Bianchi, G. Cappelletti, A. Naldoni, and C. Pirola, "Photocatalytic degradation of toluene in the gas phase: Relationship between surface species and catalyst features," *Environ. Sci. Technol.*, vol. 42, no. 17, pp. 6671–6676, 2008.

[86] L. Qiu, Y. Wang, H. Li, G. Cao, F. Ouyang, and R. Zhu, "Photocatalytic oxidation of toluene on fluorine doped TiO_2 /SiO_2 catalyst under simulant sunlight in a flat reactor," *Catalysts*, vol. 8, no. 12, p. 596, 2018.